OXFORD

*Cerebral Cortex*, 2024, **34**, 1–19
https://doi.org/10.1093/cercor/bhad431
Advance access publication date 23 November 2023
**Original Article**

# Deficits in neuronal architecture but not over-inhibition are main determinants of reduced neuronal network activity in a mouse model of overexpression of Dyrk1A

Linus Manubens-Gil[1,2,†,*], Meritxell Pons-Espinal[3,4,†], Thomas Gener[5], Inmaculada Ballesteros-Yañez[6], María Martínez de Lagrán[7], Mara Dierssen[7,8,9]

[1]Institute for Brain Science and Intelligent Technology, Southeast University (SEU), Biomedical engineering, Sipailou street No. 2, Xuanwu district, 210096, Nanjing, China,
[2]School of Biological Science and Medical Engineering, Southeast University (SEU), Sipailou street No. 2, Xuanwu district, 210096, Nanjing, China,
[3]Department of Pathology and Experimental Therapeutics, Bellvitge University Hospital-IDIBELL, Avinguda de la Granvia de l'Hospitalet, 199, 08908 L'Hospitalet de Llobregat, Barcelona, Spain,
[4]Institute of Biomedicine (IBUB) of the University of Barcelona (UB), Avda. Diagonal, 643 Edifici Prevosti, planta -108028, Barcelona, Spain,
[5]Advanced Electronic Materials and Devices Group (AEMD), Catalan Institute of Nanoscience and Nanotechnology (ICN2), CSIC and BIST, UAB Campus, Bellaterra Barcelona 08193, Spain,
[6]Inorganic and Organic Chemistry and Biochemistry, Faculty of Medicine, University of Castilla- La Mancha, Camino de Moledores, 13071, Ciudad Real, Spain,
[7]Cellular and Systems Neurobiology, Systems and Synthetic Biology Program, Center for Genomic Regulation, Dr. Aiguader 88, 08003 Barcelona, Spain,
[8]Center for Biomedical Research in the Network of Rare Diseases (CIBERER), v. Monforte de Lemos, 3-5. Pabellón 11. Planta 0 28029, Madrid, Spain,
[9]Universitat Pompeu Fabra (UPF), Dr. Aiguader 88, 08003 Barcelona, Spain

[*]Corresponding author: Institute for Brain Science and Intelligent Technology, Southeast University (SEU), Nanjing, China. Email: linusmg@seu.edu.cn
[†]Linus Manubens-Gil and Meritxell Pons-Espinal contributed equally.

In this study, we investigated the impact of Dual specificity tyrosine-phosphorylation-regulated kinase 1A (Dyrk1A) overexpression, a gene associated with Down syndrome, on hippocampal neuronal deficits in mice. Our findings revealed that mice overexpressing *Dyrk1A* (TgDyrk1A; TG) exhibited impaired hippocampal recognition memory, disrupted excitation-inhibition balance, and deficits in long-term potentiation (LTP). Specifically, we observed layer-specific deficits in dendritic arborization of TG CA1 pyramidal neurons in the *stratum radiatum*. Through computational modeling, we determined that these alterations resulted in reduced storage capacity and compromised integration of inputs, with decreased high $\gamma$ oscillations. Contrary to prevailing assumptions, our model suggests that deficits in neuronal architecture, rather than over-inhibition, primarily contribute to the reduced network. We explored the potential of environmental enrichment (EE) as a therapeutic intervention and found that it normalized the excitation-inhibition balance, restored LTP, and improved short-term recognition memory. Interestingly, we observed transient significant dendritic remodeling, leading to recovered high $\gamma$. However, these effects were not sustained after EE discontinuation. Based on our findings, we conclude that *Dyrk1A* overexpression-induced layer-specific neuromorphological disturbances impair the encoding of place and temporal context. These findings contribute to our understanding of the underlying mechanisms of Dyrk1A-related hippocampal deficits and highlight the challenges associated with long-term therapeutic interventions for cognitive impairments.

*Key words*: CA1; dendritic morphology; down syndrome; environmental enrichment; gamma oscillations.

## Introduction

Down syndrome (DS; trisomy 21) is the leading genetic cause of intellectual disability. Learning and memory impairments in DS have been attributed to synaptic dysfunction and compromised activity-dependent plasticity (Dierssen 2012). Among the genes located on human chromosome 21 (Hsa21), *Dyrk1A* (Dual-specificity tyrosine [Y]-regulated kinase) (Marti et al. 2003) has garnered attention due to its overexpression in transgenic mice (TgDyrk1A; TG), resulting in hippocampal-dependent cognitive deficits reminiscent of DS (Altafaj et al. 2001; Ahn et al. 2006). Moreover, this overexpression also leads to neuronal architecture abnormalities and reduced $\gamma$ oscillations in the cerebral cortex, further highlighting its relevance to DS (Ruiz-Mejias et al. 2016). While it has long been assumed that these microstructural alterations, combined with network over-inhibition, contribute to the cognitive impairments observed in DS (Contestabile et al. 2017; Zorrilla de San Martin et al. 2018), the exact mechanisms underlying the modification of network activity remain elusive. To bridge this knowledge gap, we employed tailored computational multicompartmental models, enabling us to investigate the impact of microstructural deficits on connectivity, activity dynamics, and the integration of inputs from the entorhinal cortex and hippocampal CA3 region onto CA1 pyramidal cells. This integration is crucial for coding place and temporal context, key processes affected in DS.

Furthermore, interventions aimed at enhancing cognitive abilities have been explored to address the structural deficits associated with DS. Environmental enrichment (EE) has demonstrated notable cognitive benefits in various models, including Ts65Dn partial trisomic DS mice (Martínez-Cué et al. 2002). In this model,

**Received:** July 4, 2023. **Revised:** October 19, 2023. **Accepted:** October 21, 2023

exposure to EE for just 1 month resulted in reduced GABAergic release (Begenisic et al. 2011), and the restoration of cognitive and neuronal impairments in the hippocampus (Pons-Espinal et al. 2013). Notably, EE induced dendritic branching and spine density rearrangements, particularly in the hippocampus (Dierssen et al. 2003). However, the functional implications of these structural changes have yet to be fully understood. Importantly, EE has been shown to increase theta-associated $\gamma$ oscillation power in the hippocampal CA1 region, particularly in the stratum radiatum, where synaptic connections between bilateral CA3 pyramidal cells occur (Shinohara et al. 2013). Given that EE also normalizes DYRK1A kinase activity and influences network activity in related brain regions, it is pertinent to investigate the specific contribution of DYRK1A to the improvements observed with EE (Martínez-Cué et al. 2002; Etter et al. 2019).

In summary, our study aims to explore the hypothesis that synaptic and structural neuronal defects in TG mice contribute to cognitive impairments by disrupting the integration of CA3 and entorhinal cortex inputs in the hippocampal CA1 region. We have identified clear structural deficits in TgDyrk1A neurons, coupled with altered excitation-inhibition balance, which were temporarily restored by EE through substantial dendritic remodeling, specifically in the distal dendritic segment of CA1 pyramidal neurons. To unravel the functional implications of these alterations, we have developed tailored computational multicompartmental models of single neurons, allowing us to examine the impact of TG-induced dendritic deficits on connectivity and activity dynamics at a layer-specific level.

# Materials and methods

## Experimental model and subject details

### *Animals*

The production of mice transgenic for *Dyrk1A* (TgDyrk1A) has previously been described (Altafaj et al. 2001). The transgene was inserted into C57BL/6JXSJL (Charles River, Barcelona, Spain) embryos and the stock is maintained by intercrossing wild type (WT) and TgDyrk1A mice derived from the original founder. The nontransgenic littermates served as controls. For the experiments to measure the width of the hippocampal layers, we generated double transgenic mice (Thy1-YFP/TgDyrk1A) by crossing TgDyrk1A (Altafaj et al. 2001) male mice with Thy1-Yellow Fluorescent Protein (YFP) females (strain B6.Cg-Tg (Thy1-YFPH)2Jrs/J n°003782; The Jackson Laboratories). Same sex littermates were group-housed under a 12-h light/dark schedule (lights on at 09:00 a.m.) in controlled environmental conditions of humidity (60%) and temperature (22 ± 2°C) with free access to food and water. The present experiments were conducted using only females, since TG male mice showed hierarchical behavior (data not shown), similar to that observed in other DS mouse models (Martínez-Cué et al. 2002) that may affect the outcome of EE. Even so, our nonenriched (NE) females showed the same phenotypes as we previously detected in TG males (Pons-Espinal et al. 2013). The nontransgenic littermates served as controls. For all the analyses we compared WT and TG mice reared in NE conditions, after 1 month of EE conditions and after EE discontinuation during 4 months. Given that EE effects after discontinuation could be confounded with age-associated changes between 2- and 6-months mice, we also assessed the age effect separately.

All experiments followed the principle of the "Three Rs": replacement, reduction, and refinement according to Directive 63/2010 and its implementation in Member States. The study was conducted according to the guidelines of the local (law 32/2007) and European regulations (2010/63/EU) and the Standards for Use of Laboratory Animals no. A5388-01 (NIH), and approved by the Ethics Committee of Parc de Recerca Biomèdica (Comité Ético de Experimentación Animal del PRBB; MDS 0035P2). Reporting followed the Animal Research Reporting of In Vivo Experiments guidelines with the modifications suggested by the Trisomy 21 Research Society for work with DS mouse models. The CRG is authorized to work with genetically modified organisms (A/ES/05/I-13 and A/ES/05/14).

### *Housing and enrichment conditions*

After weaning (21 days of age), TG and WT mice were randomly reared under either NE or enriched (EE) conditions for 30 days (Supplementary Fig. 1a). For the NE conditions, animals were reared in conventional Plexiglas cages (20 × 12 × 12 cm height) in groups of two to three animals. The EE group was reared in spacious (55 × 80 × 50 cm height) Plexiglas cages with toys, small houses, tunnels, and platforms, but without wheels to avoid the possible effects of physical exercise. The arrangement was changed every 3 days to maintain the novelty of the environment. To stimulate social interactions, six to eight mice were housed in each EE cage. All groups of animals were maintained under the same 12 h (8:00–20:00) light–dark cycle in controlled environmental conditions of humidity (60%) and temperature (22 ± 1°), with free access to food and water. To analyze the long-term stability of EE effects, after 1 month housed in EE conditions, a separate group of WTEE (WTEE discontinued; WTEEdis) and TGEE (TGEE discontinued; TGEEdis) mice was reared for 4 months under NE conditions (Supplementary Fig. 1b).

## Method details

### *Novel object recognition test*

The novel object recognition test is widely used to assess recognition memory in rodents (Broadbent et al. 2009). Briefly, mice were placed into an open-field (70 cm wide × 70 cm long × 30 cm high) made of black methacrylate, surrounded by curtains. The task was performed under nonaversive low lighting conditions (50 lux). An overhead camera connected to video-tracking software (SMART, Panlab) was used to monitor the animal's behavior. To eliminate odor cues, the arena and the objects were thoroughly cleaned with 10% odorless soap, and dried. In addition, the positions of the objects in the familiarization and test session were counterbalanced between animals. Sniffing of the objects was used as a measure of exploration and was registered manually by an experimenter blind to genotype and treatment. The first day, mice were allowed to explore the arena for 5 min for familiarization with the experimental setting. Thereafter, an object was placed in the center of the arena, and mice were given the chance to habituate. Exploration of the object was recorded for 5 min. On the second day (Supplementary Fig. 1c), during the familiarization trial, mice were allowed to explore two identical objects placed in the center of the apparatus for 10 min. Mice exploring <20 s were discarded. One hour after, during the test session, mice were allowed to explore the same arena for 5 min, but with one of the familiar objects exchanged by a new one. The exploration times for the familiar and new object during the test phase were recorded (number of animals: WTNE = 14; TGNE = 15; WTEE = 16; TGEE = 19 and after EE discontinuation: WTNE = 11; TGNE = 14; WTEEdis = 18; TGEEdis = 18). Memory was operationally defined as the discrimination index, defined as the time spent investigating the novel object minus the time spent investigating the familiar one during the testing period [Discrimination Index = [(Exploration Time New – Exploration Times Familiar)/Total Exploration Time] × 100].

### *Neuromorphological analysis*

The structural changes were analyzed on the dorsal hippocampal CA1 layer (Paxinos and Franklin 2019) (Mouse Brain Atlas: antero-posterior = −1.34 to −2.54 mm; medio-lateral 0.5–1.6 mm; dorso-ventral 1.2–2 mm; Supplementary Video 1) of Thy1-YFP/TgDyrk1A (TG) and Thy1-YFP/WT. Data from the left and right hemispheres were taken indistinctly.

### Layer width analysis of hippocampal CA1 strata

Mice were sacrificed and perfused intracardially with phosphate buffered saline (PBS), followed by chilled 4% paraformaldehyde (Sigma). The brains were removed from the skull, postfixed in the same fixative at 4°C overnight, and cryoprotected in 30% sucrose. About 150 $\mu$m coronal brain sections were obtained using a vibratome (VT1000S, Leica Microsystems), washed extensively with 0.1 M PBS, and mounted and coverslipped with mowiol (number of slices/animals: WTNE = 14/5; TGNE = 8/4; WTEE = 17/6; TGEE = 8/3) and 4 months after termination of EE treatment to evaluate the long-term stability of EE effects (number of slices/animals: WTNE = 24/8; TGNE = 9/4; WTEEdis = 18/6; TGEEdis = 19/7).

Images of the dorsal hippocampal CA1 region were obtained using a confocal microscope (SPE; Leica Microsystems) with a 10× objective. A line scan of 1,024 × 1,024 pixels, 3 $\mu$m wide z steps and three frame intensity averages were used. An average projection was generated with the Fiji imaging analysis software (version 2.9.0/1.53t) (Schindelin et al. 2012). Image stacks of slanted vibratome sections were discarded for subsequent analysis.

The width of the *stratum radiatum* (intercept between the *stratum pyramidale-radiatum* border and the *radiatum-lacunosum* border) and *stratum lacunosum* (intercept between the *stratum radiatum-lacunosum* border and the hippocampus sulcus), where apical dendrites of CA1 pyramidal neurons are located, were analyzed at four medio-lateral locations (Paxinos and Franklin 2019) (Bregma, antero-posterior = −1.06 to −2.54 mm; medio-lateral 0.5–1.6 mm) using the Fiji straight line selection tool. The four locations were equispaced by ∼200 $\mu$m from proximal to distal along the medio-lateral axis (Supplementary Fig. 2).

### Single-cell morphological analysis of dendritic tree architecture of hippocampal pyramidal cells

To reconstruct dendritic tree architecture of single CA1 pyramidal cells, TG animals were perfused with 4% paraformaldehyde, and 150 $\mu$m coronal sections from the dorsal hippocampal CA1 region (Bregma, antero-posterior = −1.06 to −2.54 mm; medio-lateral 0.5–1.6 mm) were obtained with a vibratome. Intracellular injections were performed in CA1 pyramidal neurons by continuous current of fluorescent Lucifer Yellow as described in detail in Elston et al. (Elston and Rosa 1997; Elston et al. 2001). Briefly, pyramidal neurons located randomly throughout the dorsal CA1 area (Paxinos and Franklin 2019) (Bregma, antero-posterior = −1.06 to −2.54 mm; medio-lateral 0.5–1.6 mm) were selected for Lucifer Yellow injection and further reconstruction (number of neurons/animals: WTNE = 18/4; TGNE = 19/4; WTEE = 19/4; TGEE = 15/3 and WTNE = 18/5; TGNE = 18/5; WTEEdis = 18/3; TGEEdis = 18/4). With a preliminary set of reconstructions ($N = 6$ for WTNE and TGNE) we did a sample size estimation based on the total length measured in those neurons ($mL_{WT} = 1637$, $mL_{TG} = 1066$, standard deviation = 536). A sample size of $N = 14$ would have a Type I error rate of 0.05 and a power of 0.80. The sections were then counter-stained with antibodies against Lucifer Yellow. Sections were washed with PBS and 0.3% Triton PBS to make the cells permeable. To minimize the background staining, the slices were treated with 50 mM glycine (minimum 99% TLC, Sigma-Aldrich, St. Louis, MO, USA) in 0.3% Triton PBS for 20 min. Thereafter, samples were treated for 2 h at room temperature with 3% bovine serum albumin (BSA, Sigma-Aldrich, St. Louis, MO, USA), and 0.3% Triton PBS as a blocking agent, and were incubated overnight at 4°C in polyclonal rabbit IgG fraction anti-Lucifer yellow (1:500, Life Technologies—Thermo Fisher Scientific, RRID:AB_2536190) in 0.3% Triton PBS and 1% BSA. The slices were then incubated 2 h at room temperature in goat anti-rabbit IgG 488 (1:200, Invitrogen—Thermo Fisher Scientific, RRID:AB_2576217, Carlsbad, California, USA) in 1% BSA in 0.3% Triton PBS. Finally, sections were washed with 0.3% Triton PBS and PBS and coverslipped with mowiol mounting medium.

Image analysis and neuronal reconstruction: Images of single neuron apical trees for neuronal reconstruction were acquired with a confocal microscope (SP5 Upright; Leica Microsystems) with a 20× air objective (HCX PL APO CS 20.0 × 0.70 dry UV). A line scan of 1,024 × 1,024 pixels, 0.347 $\mu$m wide z steps and three-line intensity averages were used for imaging whole dendritic trees. Leica Smart Gain was used to equalize the fluorescence signal intensity in depth in the samples. The signal to noise ratio was measured for each stack at a 100 $\mu$m depth for a representative dendritic segment and an equivalent area containing only background at the same depth. Images with signal-to-noise ratio <1.5 were discarded for subsequent analysis. 2D gaussian blurring was applied to the stacks with a sigma of 2 pixels https://imagej.nih.gov/ij/developer/api/ij/plugin/filter/GaussianBlur.html, background subtraction (50 pixel sliding paraboloid without smoothing; https://imagej.net/Rolling_Ball_Background_Subtraction) and contrast enhancement (with 0.3% saturated pixels and using the stack histogram; https://imagej.nih.gov/ij/developer/api/ij/plugin/ContrastEnhancer.html) in Fiji.

Dendritic trees were reconstructed with NeuTube (version 1.0z.2018.07) (Feng et al. 2015). Morphological metric statistics were obtained with the TREES Toolbox (version 1.15) function stats_tree, documented in detail at https://www.treestoolbox.org/manual/stats_tree.html (Cuntz et al. 2011). Briefly, the function provides a set of measurements that describe in detail morphological properties of the dendritic tree: total length, maximum and mean path length, mean branch length, dendritic spanning volume, number of branch points, maximum and mean branching order, dendritic area (surface occupied by dendrite), mean straightness of dendritic branches, mean branching angle, mean asymmetry, center of mass in different directions and the ratio between width and height (see Supplementary Table 1 for details). We measured the extent of the reconstructed neurons within CA1 *stratum radiatum* and *lacunosum* by aligning the apical tree in the dorso-ventral direction. Additionally, the stats_tree function allows us to obtain the Sholl analysis for each of the trees. For our analyses we used 20 $\mu$m separation between consequent Sholl spheres at which the number of intersections were quantified. The data were plotted using the ggline of the R (version 4.1.0) package ggpubr (version 0.4.0).

### Dendritic spine density and morphology

Images from the Lucifer Yellow-injected CA1 pyramidal neurons used to analyze dendritic spine density and morphology from single neuron reconstructions were acquired with a confocal microscope (SPE; Leica Microsystems) using a 63× oil objective (ACS APO 63.0 × 1.30 oil) plus five times magnification. A line scan of 1,024 × 1,024 pixels, 0.1 $\mu$m wide z steps and three frame intensity averages were used for imaging dendritic segments.

Representative images were obtained by 3D rendering of the confocal imaging stacks in the Imaris software (Bitplane) after image deconvolution using Huygens (version 15.05; Scientific Volume Imaging). The resulting dendritic spine images were quantified with the aid of Fiji.

Dendritic spine density was measured by quantifying the number of spines in 20 $\mu$m length dendritic segments located 30 $\mu$m distal from the soma of Lucifer Yellow-injected CA1 pyramidal cells in 60%–70% of neurons reconstructed (number of dendrite segments/neurons reconstructed/animals analyzed: WTNE = 19/19/4; TGNE =16/12/4; WTEE = 19/19/4; TGEE = 16/9/4 and after EE treatment discontinuation: WTNE = 20/20/4; TGNE = 19/19/5; WTEEdis = 18/18/3; TGEEdis = 18/18/6). Spines were classified as filopodia (type A), immature (type B), or mushroom (type C) (Fig. 2i).

### Excitation-inhibition balance analysis

In a separate experiment, mice were sacrificed, and perfused intracardially as detailed above (number of animals analyzed: WTNE = 7; TGNE = 7; WTEE = 8; TGEE = 7 and after EE treatment discontinuation: WTNE = 5; TGNE = 6; WTEEdis = 5; TGEEdis = 4). About 40 $\mu$m coronal sections were obtained using a cryostat (CM3050S, Leica Microsystems). Analysis was performed in one of every six sections (6–8 sections per animal), covering the dorsal hippocampus (Paxinos and Franklin 2019) (Bregma, antero-posterior −1.06 to −2.54 mm; medio-lateral 0.5–1.6 mm). Free-floating brain sections were permeabilized with 0.3% Triton X-100 in PBS for 30 min at room temperature (RT), and blocked with 20% fetal bovine serum and 0.3% Triton X-100 in PBS for 1 h at RT. Subsequently, sections were incubated overnight at 4°C with the primary mouse anti-vesicular glutamate transporter 1 (VGLUT1) antibody (1:200, Synaptic Systems, RRID:AB_887879) to analyze presynaptic excitatory punctae and the guinea pig anti-vesicular GABA transporter (VGAT) antibody (1:200, cytoplasmic domain, Synaptic Systems, RRID:AB_887871) to evaluate presynaptic inhibitory punctae. The following day, while protected from light, slices were incubated with the corresponding secondary fluorescent antibodies (1:1000, Alexa 488 RRID:AB_2535764 and 555 RRID:AB_141784, Invitrogen) for 1 h at RT.

Four images per section (8 sections per animal) were captured in the *stratum radiatum* of CA1 hippocampal subfield using a confocal microscope with a 63× objective (ACS APO 63.0 × 1.30 oil) and 5× magnification (SPE; Leica Microsystems). High-resolution images (pixel size = 0.034 × 0.034 $\mu$m) were obtained and imported into Fiji and the negative control background intensity of each image was subtracted from each channel. To identify immunopositive punctae, the preprocessed images were thresholded and binarized using the Threshold command in Default mode. The number of VGLUT1 and VGAT puncta within the *stratum radiatum* area in CA1 were counted with a particle analysis plug-in of ImageJ using a defined puncta size range.

## Modeling the functional consequences of dendritic remodeling

### *Connectivity repertoire*

To study putative functional implications of genotype and treatment-dependent changes in dendritic architecture and spine density, we analyzed the connectivity repertoire $S$ of the reconstructed neurons, defined as the possible connectivity patterns between dendrites and surrounding axons (Wen et al. 2009). Specifically, we explored whether the genotype and/or treatment-dependent differences in neuronal shapes affect the repertoire of possible connectivity patterns between dendrites and surrounding axons. Briefly, following (Wen et al. 2009) we measured total dendritic length with the *stats_tree* function of the TREES toolbox and the arbor radius $R$ with a self-developed MATLAB script that provided the root mean square distance between any two dendritic segments from the 3D apical pyramidal dendrites reconstructions described above:

$$R^2 = \frac{1}{L^2}\sum_{i=1}^{k}\sum_{j=1,j\neq i}^{k}\delta l_i \delta l_j (r_i - r_j)^2 \quad (1)$$

Being $L$ the total length, $k$ the total number of segments, $\delta l_i$ the length of the segment $i$ and $r_i$ the position vector of the segment $i$. To obtain a quantification of the connectivity repertoire as a function not only of the dendritic tree morphology but also the density of synaptic contacts, which are strongly affected by the genotype and EE, we introduced spine densities measured in each group in the calculation of $S$ by scaling the number of inputs in the tree $N$ by the spine density $s_d$ resulting in the following equation:

$$S \simeq \mathrm{MH}(\mathrm{W}) + \frac{L}{a}\left(1 + \log\left(1 - \frac{R}{l}\right)\right) - \frac{l^2}{La} - s_l s_d \frac{L^2}{R^2} \quad (2)$$

### *Input–output frequency relation*

We also investigated whether the genotype and treatment-dependent dendritic remodeling affect the efficiency of WT and TG trees to integrate synaptic signals. To this aim we explored the input–output frequency relationship defined as the evoked spiking frequency of a neuron upon the activation of 15% of available input synapses at different frequencies (from 0 to 100 Hz in steps of 10 Hz), since CA1 dendritic trees have been shown to lock at constant low gamma output frequency of 50 Hz for high gamma input frequencies (ranging from 50 to 100 Hz) at their *stratum radiatum* (Combe et al. 2018). We based our model on (Combe et al. 2018) (with ID in the ModelDB database NRNID 244416), in which the authors explore selective firing frequency of CA1 pyramidal neurons upon stimulation of Schaffer collateral input. They observed linear response for input frequencies between 0 and 40 Hz, and selective firing at slow gamma for input frequencies between 40 and 100 Hz. Membrane channel conductances and distributions were mimicked from the template model. We modified the synaptic weight, following experimental measurements obtained in CA1 pyramidal neurons of the mouse (Lipina et al. 2016). We explored systematically the percentage of active synapses and found that 15% best recapitulate the behavior of the original model (spike-time adaptation as observed in electrophysiological experiment in mouse CA1) after updating the values of synaptic weights. In addition to the Schaffer collateral input to *stratum radiatum*, we also included perforant path synapses in *stratum lacunosum* in order to explore whether summation of both inputs would lead CA1 neurons to modify their firing frequencies to high gamma (Jarsky et al. 2005).

To model this behavior computationally, we used the NEURON simulation environment (version 7.7.1) and T2N (version 1.13.1) (Beining et al. 2017) in MATLAB (R2021a). T2N is an extension of the TREES toolbox, that allows to define passive and active membrane electrophysiological properties (i.e. passive currents, active ion channels, synaptic inputs, etc.) depending on the position within a neuronal reconstruction and export a multicompartmental model in NEURON format, to simulate

neuron dynamics upon injection of currents. In our case, as we were particularly interested in the impact of synaptic input currents in CA1 *stratum radiatum*, we introduced electrophysiological parameters as defined in the NEURON CA1 neuron model of Combe et al. (2018). We generated an individual neuron dynamics model for each reconstructed dendritic tree accounting for a leak current, two fast Hodgkin-Huxley-type $Na^+$currents (somato-dendritic and axonal), a delayed rectifier, two A-type $K^+$ currents (proximal and distal), an M-type $K^+$ current, a mixed conductance hyperpolarization-activated h-current, a T-type $Ca^{2+}$ current, an R-type $Ca^{2+}$ current, two L-type $Ca^{2+}$ currents (somatic and dendritic), a slow $Ca^{2+}$-dependent $K^+$ (SK) current and a $Ca^{2+}$- and voltage-dependent $K^+$ (BK) current.

To introduce synaptic currents, we accounted for the differences in spine density and length of the dendritic compartments between genotypes and conditions in order to position synaptic currents accordingly. Given that spine density was measured in 20 $\mu$m length dendritic segments, to obtain more realistic electrophysiological dynamics throughout dendritic branches, we accounted for the previously described linear decrease of synaptic weight from the trunk to the tips CA1 apical dendrites (Katz et al. 2009). We scaled the weight of each synapse by the branch level order (summed path distance of all child branches to the root of the tree, https://www.treestoolbox.org/manual/LO_tree.html), which is minimal on the tips of the branches and maximal close to the trunk. Synaptic weight values were scaled by the level order in each point of the tree and normalized to maximal and minimal values of 0.6 and 0.4 spines per $\mu$m respectively based on Katz et al. (Katz et al. 2009).

### *Averaged activity upon inhibitory feedback*

To assess the impact of inhibition on the spiking frequency of CA1 neurons we extended our multicompartmental models to include somatic inhibitory synapses. A pair of inhibitory neurons was simulated for each CA1 pyramidal cell to account for both inhibition of inhibitory and excitatory neurons (Ferrante et al. 2009). Artificial integrate-and-fire inhibitory neurons were defined using the T2N IntFire2 structure. The number of inhibitory synapses was set based on known proportions of synapses in CA1 pyramidal and Parvalbumin neurons (Megias et al. 2001). Specifically, we approximated the proportion of inhibitory to excitatory synapses in pyramidal CA1 cells as 1–15, and multiplied this value to the VGLUT1/VGAT ratio we measured experimentally. To take into account the fact that Parvalbumin neurons receive approximately half of the synapses received by pyramidal cells, we introduced half the number of synapses to the inhibitory virtual neurons. To explore how the averaged activity of different cells could coordinate their activity through inhibition, individual pyramidal cells were stimulated with regular 100 Hz spike trains in 7.5% available synapses for 1 s. One multicompartmental model was generated for each neuron. The somatic activity was measured in the model and spike times were recorded. The averaged activity power spectrum for each group was quantified by pooling the spike times of all the simulated neurons in a single array and obtaining its Fourier transform. The code for the multicompartmental model simulations can be found at https://github.com/lmanubens/EE_CA1/tree/main/model.

## Electrophysiological recordings

Field excitatory postsynaptic potentials (fEPSPs) were recorded in the *stratum radiatum* of the dorsal hippocampal CA1 region (Paxinos and Franklin 2019) (Bregma, antero-posterior −1.06 to −2.54 mm; medio-lateral 0.5–1.6 mm), in response to stimulation of the Schaffer collateral pathway in WT and TG mice reared in NE conditions and after 1 month of EE conditions (number of slices/animals: WTNE = 11/5; TGNE = 11/5; WTEE = 9/5; TGEE = 16/5). The same analysis was performed in WT and TG mice reared under NE conditions for 4 months after termination of EE treatment to evaluate the long-term stability of EE effects (number of slices/animals: WTNE = 16/5; TGNE = 13/6; WTEEdis = 15/7; TGEEdis = 16/5). Following decapitation, the brain was quickly removed, placed on ice-cold cutting solution (in mM: KCl 2.5; $MgSO_4$ 3; $NaHPO_4$ 1.25; $CaCl_2$ 1; $NaHCO_3$ 26; sucrose 10) and gassed with 95% $O_2$–5% $CO_2$ to a final pH of 7.4. About 400 $\mu$m thick coronal slices were obtained with a vibratome (Leica). The slices were then placed in an interface style recording chamber (Fine Science Tools) and bathed in artificial cerebrospinal fluid (ACSF, in mM: NaCl, 124; KCl, 2.5; $MgSO_4$, 1; $NaHPO_4$, 1.25; $CaCl_2$, 2.5; $NaHCO_3$, 26; dextrose, 10), and then aerated with 95% $O_2$–5% $CO_2$ to a final pH of 7.4. Bath temperature was maintained at 32–34°C. Unfiltered recordings were obtained by means of glass electrodes (impedance 1–2 M$\Omega$) through a Neurolog system (Digitimer) amplifier. Electrical stimuli were delivered with a concentric bipolar electrode (platinum-iridium) with the stimulus strength adjusted to a stimulation intensity that yielded a half-maximal response. For each slice, after determining a stable baseline, paired-pulse facilitation (PPF) was induced by a double-pulse (50 ms apart) stimulation protocol and represented as the ratio of both stimuli (fEPSP2/fEPSP1). After 15 min of baseline registering (pulse at 0.016 Hz), long-term potentiation (LTP) was induced via theta burst stimulation (TBS) (five episodes at 0.1 Hz; one episode was 10 stimulus trains of four pulses at 100 Hz; delivered at 5 Hz) and registered for 60 min (pulse at 0.016 Hz). Data are represented as the percentage of the baseline response. Recordings were digitized, acquired, and analyzed using a data acquisition interface, and software from Cambridge Electronic Design (Spike2; version 6.18).

## Dyrk1A kinase activity assay

Dyrk1A kinase activity was measured in the hippocampus (number of animals: WTNE = 11; TGNE = 9; WTEE = 10; TGEE = 10 and after EE discontinuation: WTNE = 12; TGNE = 12; WTEE = 12; TGEE = 11) as previously described (Pons-Espinal et al. 2013). Briefly, samples were extracted in a Hepes lysis buffer and immunoprecipitated with a mouse anti-Dyrk1A antibody (Abnova RRID:AB_1574529; 3 $\mu$g/sample) immobilized on glutathione-sepharose beads (GE Healthcare). The recovered samples were analyzed by immunoblotting and in vitro kinase assays.

To determine the catalytic activity of Dyrk1A, 500 $\mu$g of the purified protein were incubated for 50 min at 30°C in 30 $\mu$L of phosphorylation buffer containing 2 mM of specific Dyrk1A peptide (Himpel et al. 2000) [DYRKtide-RRRFRPASPLRGPPK], 1 mM ATP, and [$\gamma$-32P]ATP (2 $\mu$Ci/sample). About 5 $\mu$L of reaction aliquots were dotted onto P81 Whatman paper. After washing extensively with 5% phosphoric acid, counts were determined in a liquid scintillation counter. Relative kinase activity was obtained, normalizing against the amount of Dyrk1A protein present in the immunocomplexes. Immunocomplexes were resolved by 7.5% SDS-PAGE, transferred onto a nitrocellulose membrane and incubated with anti-Dyrk1A antibody (1/1,000) overnight at 4 °C. After that, membranes were incubated for 1 h at RT with the corresponding secondary antibody. Detection was performed using ECL (GE Healthcare) and determined with LAS-3000 image analyzer (Fujifilm Image Reader V2.2; Fuji PhotoFilm). Protein quantification was performed using Image Gauge software version 4 (Fuji PhotoFilm).

## Quantification and statistical analysis

Data were plotted as mean ± standard error of the mean (SEM) or ±standard deviation and analyzed using the multivariate analysis of variance (MANOVA) for the statistical analysis of four groups containing two independent variables (genotype and treatment). Bonferroni-Holm was used for post hoc analysis when a significant, or a trend to ($P < 0.09$) genotype × treatment interaction was found. For those experiments with repeated events, comparisons were performed using MANOVA repeated measures. For structural analysis data we used an unbalanced block design, which allows an unequal number of observations per group (in our case, numbers of neurons reconstructed per genotype and/or treatment). In this case we used a mixed-effect linear model with the residual maximum likelihood (REML) method and blocked for biological replicates. *P*-values were obtained from the adjusted denominator degrees of freedom for linear estimates and *t* distributions calculated using the Kenward-Roger approximation (mixed function in the afex R package, version 0.28-1), adjusting pairwise comparisons with Bonferroni-Holm as post hoc. All the analyses were performed using R (version 4.1.0) and its packages stats (version 4.1.0) and emmeans (version 1.6.1). Results were considered significant when $P < 0.05$ and trends were considered when $P < 0.1$. All the metrics and analyses are available in an in-house developed Shiny App (version 1.6.0; https://linusmg.shinyapps.io/EE_TgDyrk1A/).

# Results

## Environmental enrichment improves cognitive performance, and partially rescues levels of DYRK1A kinase activity, dendritic complexity, and spine morphology in young (2-months) TgDyrk1A

We tested the effects of genotype and EE using the novel object recognition paradigm in 2-month-old (2mo) mice. TgDyrk1A (TG) NE showed impaired hippocampal recognition memory, with reduced novel object discrimination (discrimination index; DI) compared to WT (Fig. 1a) with no genotype-dependent differences in total time of exploration in the training session (see Shiny app https://linusmg.shinyapps.io/EE_TgDyrk1A/ for interactive analysis). This impairment in discrimination index was rescued by 1 month of EE (Fig. 1a). EE did not show effects in WT mice (Fig. 1a; WTEE vs. WTNE, N.S.). Hippocampal DYRK1A kinase activity showed a significant genotype-treatment interaction (Fig. 1b), but pairwise comparisons for WTNE versus TGNE and TGEE versus TGNE were not statistically significant.

Reconstructions of pyramidal CA1 neurons in NE mice showed altered global neuronal architecture with a significant reduction in the dorso-ventral span (see Methods and Supplementary Fig. 1), i.e. the length from cell body to apical tuft in TGNE mice (Fig. 1c and d). We also detected a reduction in the width of the *stratum radiatum*, the postsynaptic target site of CA3 excitatory neurons, but not in the *stratum lacunosum-moleculare*, which receives temporo-ammonic projections (Supplementary Fig. 3a–c). EE rescued the reduction of dorso-ventral span of TG CA1 neurons (Fig. 1d), but did not induce significant changes in WT neurons. We also found a significant dendritic remodeling of the dorso-ventral span upon EE (Supplementary Fig. 3a–c). However, post hoc pairwise comparisons were not significant for either TGEE versus TGNE nor WTEE versus WTNE. The maximum path length, e.g. the length of the longest (primary) dendrite, was significantly reduced in TGNE neurons and recovered by EE treatment (Supplementary Fig. 4a), but again EE did not have significant effects on WT neurons.

Dendritic tree complexity was also reduced in TGNE CA1 neurons (Fig. 1c and e and Supplementary Fig. 4b). EE increased dendritic complexity in both TG and WT dendritic trees (Fig. 1e and Supplementary Fig. 4b). The Sholl AUC was 52% larger in TGEE than in TGNE and 36% in WTEE compared to WTNE.

Finally, we did not observe differences in the total density of dendritic spines between genotypes (Fig. 1f and Supplementary Fig. 3). However, TGNE mice showed reduced mature mushroom-like spines (Fig. 1f–h) along with increased thin immature spines. Regarding dendritic spines, the effects of EE were different in TG and WT. In TG neurons EE did not change total spine density but slightly increased mushroom-like spines (Fig. 1f and h), at the expense of a significant reduction of thin spines (Fig. 1f and h). In WT mice, EE did not produce any significant change nor any trend in the density of spines of any type.

In summary, EE rescued the cognitive impairment and hippocampal DYRK1A kinase activity in TG mice at 2mo of age. CA1 *stratum radiatum* width defects were partially rescued by EE, which mainly increased dendritic complexity in both genotypes, whereas it possibly favored spine maturation and stabilization in TG mice.

## Deficits in LTP and excitation-inhibition balance in young TG CA1 are rescued by EE

Extracellular field recordings on the Schaffer collateral-CA1 synapse of hippocampal slices measuring field excitatory postsynaptic potentials (fEPSPs) showed a significant genotype effect with reduced paired pulse facilitation (PPF, the ratio of a double-pulse stimulation fEPSP2/fEPSP1) in 2mo TG mice (Fig. 2a), indicating an impairment of presynaptic function in TG mice. After TBS on the Schaffer collateral pathway, TGNE showed a significant deficit in hippocampal CA1 LTP (Fig. 2b). Upon EE, PPF was significantly increased in both genotypes (Fig. 2a). Importantly, EE completely recovered the fEPSP slope (Fig. 2b) and rescued the reduced LTP response in TG CA1.

Given that impaired synaptic plasticity in DS may result from an excitation-inhibition imbalance (Belichenko et al. 2004; Kleschevnikov et al. 2004), we analyzed the ratio of excitatory (vesicular glutamate transporter 1, VGLUT1+) and inhibitory (vesicular GABA transporter, VGAT+) presynaptic puncta (Fig. 2c). TGNE 2mo mice showed a significantly reduced VGLUT1/VGAT ratio (Fig. 2d), indicating a bias toward inhibition in presynaptic transmission, due to reduced density of VGLUT1 puncta with no changes in VGAT density (Fig. 2c and d). EE increased VGLUT1/VGAT ratio in both genotypes, leading to a complete recovery of the excitatory-inhibitory imbalance in TGEE mice (Fig. 2c and d) due to the increase in VGLUT1 density (Fig. 2d). See Supplementary Table 2 for values of puncta density per unit of area (1,000 $\mu m^2$).

## Connectivity repertoire and input–output frequency deficits in young TG mice are partially rescued by environmental enrichment

To ascertain the potential impact of the dendritic architecture and spine density disruptions observed in 2mo TG CA1 pyramidal neurons on their topological properties, we quantified the repertoire of their possible connectivity patterns (Equation (2), connectivity repertoire; Wen et al. 2009). To elucidate the specific role of spine density in shaping the connectivity repertoire, we performed calculations by assuming that all experimental groups possessed

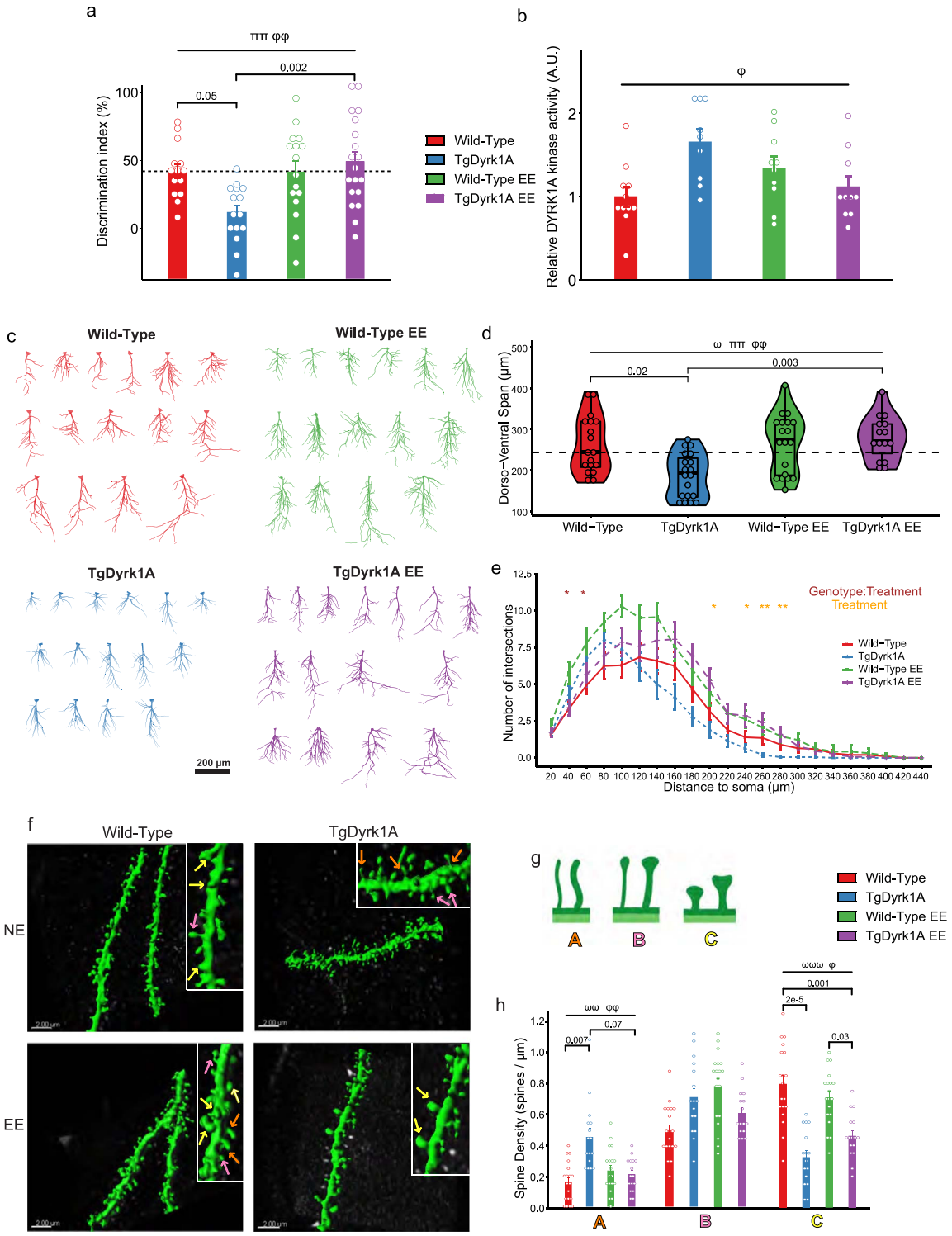


**Fig. 1.** EE improves cognitive performance, and partially rescues levels of DYRK1A kinase activity, dendritic complexity and spine morphology in 2mo TgDyrk1A (TG). a) Discrimination index (%) during the test session of the NOR paradigm in WT and TgDyrk1A (TG) mice reared for 1 month under NE or environmentally enriched (EE) conditions. Number of animals analyzed: WTNE (2mo) = 14; TGNE (2mo) = 15; WTEE (2mo) = 16; TGEE (2mo) = 19. b) Relative DYRK1A kinase activity in the hippocampus. Number of animals analyzed: WTNE (2mo) = 11; TGNE (2mo) = 9; WTEE (2mo) = 10; TGEE (2mo) = 10. For a and b Data are expressed as mean ± SEM. Two-way ANOVA treatment effect $\pi\pi$ $P < 0.01$. Two-way ANOVA genotype-treatment interaction $\varphi\varphi$ $P < 0.01$. c) 2D projection of reconstructed apical dendritic trees in 2mo WT and TG, NE and EE. Scale bar = 200 $\mu$m. d) Length of CA1 apical dendritic trees along the dorso-ventral axis (single cell measurement). Data are presented as an overlay of dot plots, boxplots and violin plots. Dotted line indicates the median value of the WTNE (2mo) group. Number of neurons/animals: WTNE (2mo) = 18/4; TGNE (2mo) = 19/4; WTEE (2mo) = 19/4; TGEE (2mo) = 15/3. Linear mixed effects: treatment effect $\pi\pi$ $P < 0.01$. e) Sholl analysis. Lines indicate mean ± SEM. Linear mixed effects, *$P < 0.05$, **$P < 0.01$. f) Representative confocal images showing CA1 apical dendritic spines in 2mo WT and TG mice under NE or EE conditions. Scale bar = 2 $\mu$m. Right upper insert corresponds to a higher magnification. Orange, pink and white arrows denote type A, type B and type C spines, respectively (see g). g) Illustration of the morphological categories used to classify spines. h) Density of each spine type. Data are expressed as mean ± SEM. Number of dendrite segments/neurons/animals analyzed: WTNE (2mo) = 19/19/4; TGNE (2mo) =16/12/4; WTEE (2mo) = 19/19/4; TGEE (2mo) = 16/9/4. Linear mixed effects: genotype effect $\omega\omega$ $P < 0.01$; $\omega\omega\omega$ $P < 0.001$; genotype × treatment interaction $\varphi$ $P < 0.05$; $\varphi\varphi$ $P < 0.01$.

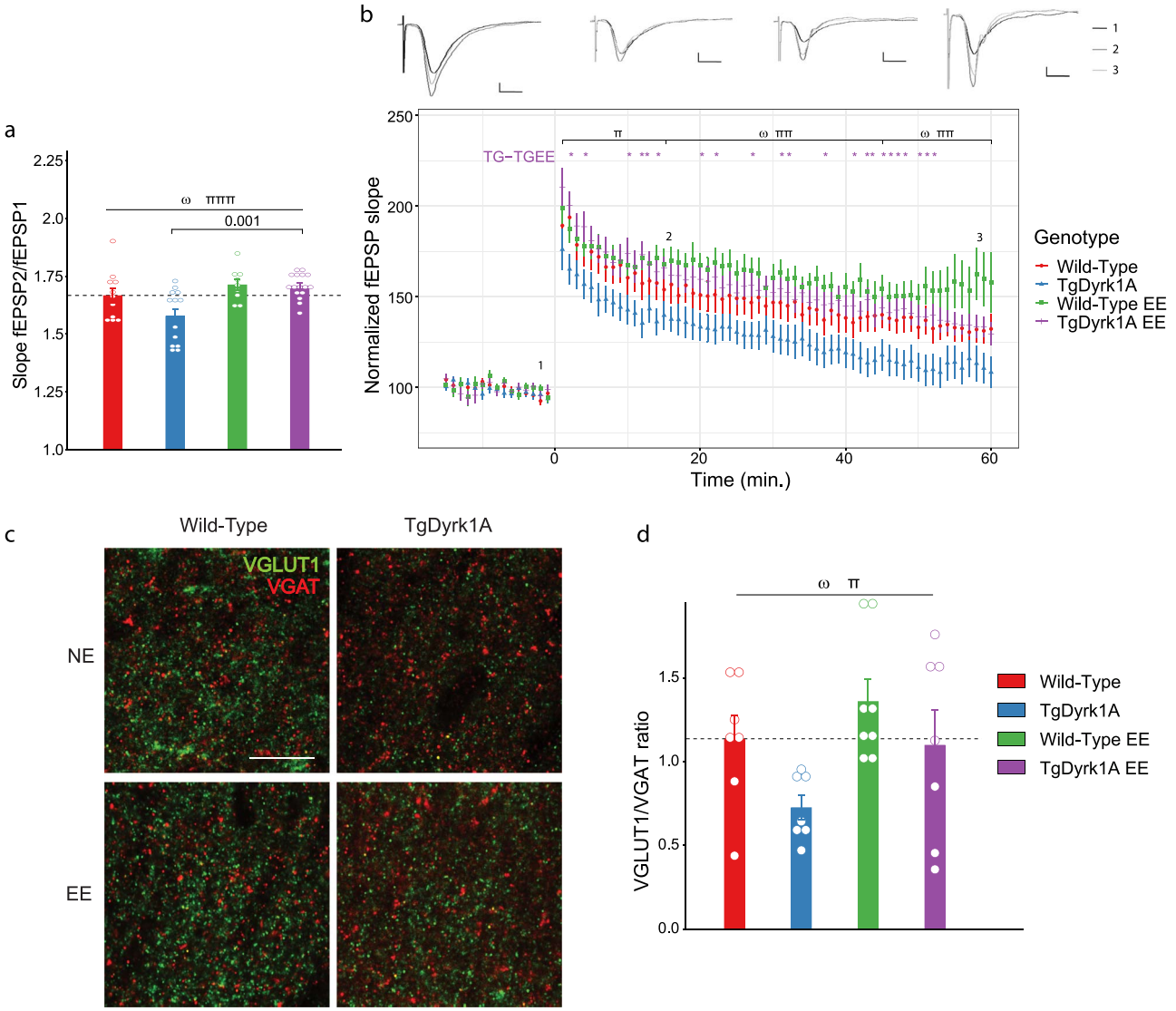


**Fig. 2.** Deficits in LTP and excitation-inhibition balance in TG CA1 are rescued by EE. a) Paired pulse facilitation (fEPSP2/fEPSP1) in the hippocampus of WT and TG mice reared under NE or EE conditions (slices/animals: WTNE (2mo) = 11/5; TGNE (2mo) = 11/5; WTEE (2mo) = 9/5; TGEE (2mo) = 16/5). Two-way repeated measures ANOVA genotype effect $\omega$ $P < 0.05$; treatment effect $\pi\pi\pi$ $P < 0.001$. b) LTP in CA1 induced by TBS in CA3 under NE or EE conditions at 2 months of age (number of slice/animals: WTNE (2mo): 11/5; TGNE (2mo): 14/5; WTEE (2mo): 14/6; TGEE (2mo): 16/5). Upper panel: representation of the mean of five responses to a stimulation at time 1 (−5 min), 2 (15 min) and 3 (60 min). Vertical bar represents 500 $\mu$V, horizontal bar represents 5 ms. lower panel: Normalized fEPSP slope before and after TBS. black horizontal bar represents 2 ms. Two-way repeated measures ANOVA genotype effect $\omega$ $P < 0.05$; treatment effect $\pi$ $P < 0.05$; $\pi\pi$ $P < 0.01$. c) Representative confocal images showing VGLUT1+ and VGAT+ puncta in CA1 *stratum radiatum* hippocampal subfield. Scale bar = 10 mm. d) Histogram showing the VGLUT1+/VGAT+ ratio. Data are expressed as mean ± SEM. WTNE (2mo) $n = 7$; TGNE (2mo) $n = 7$; WTEE (2mo) $n = 8$; TGEE (2mo) $n = 7$. Two-way ANOVA genotype effect $\omega$ $P < 0.05$; treatment effect $\pi$ $P < 0.05$.

the WT density of mature spines. Interestingly, when considering solely the reduced dendritic span and complexity observed in TGNE neurons, we found that the connectivity repertoire did not significantly differ from that of the WTNE group (Supplementary Fig. 5a). However, when considering the reduction in mature spine density, we observed a significant decrease of connectivity repertoire in TGNE neurons compared to WTNE neurons (Supplementary Figs. 6a and 5b). Following exposure to EE, we observed a substantial increase in dendritic tree span and complexity in both WTEE and TGEE neurons (see Fig. 1d and e). Importantly, this enhancement was significant and led to a notable expansion of the connectivity repertoire specifically in TGEE neurons (Supplementary Fig. 5a). Furthermore, when considering the concurrent increase in mature dendritic spines following EE, we found that the expansion of the connectivity repertoire remained significant (Supplementary Figs. 6a and 5b). Thus, the observed increase in connectivity repertoire in TGEE neurons can be attributed not only to the augmentation of dendritic tree span and complexity but also to the concurrent increase in mature dendritic spines.

Given that a reduced connectivity repertoire can have implications for neuronal signal integration (Chklovskii et al. 2002), we investigated the input–output relationship of individual CA1 pyramidal neurons using multicompartmental models. These models enabled us to simulate the complete dendritic tree spanning the *stratum radiatum* and *stratum lacunosum-moleculare*, or alternatively, the dendritic area exclusively covering the *stratum radiatum*. Since the CA1 region has a tendency to synchronize with either CA3 or the medial entorhinal cortex at distinct frequencies, we were able to model the input–output characteristics of the *stratum radiatum*, which serves as the postsynaptic target site for CA3 excitatory

neurons, and the *SL*, which receives projections from the temporoammonic pathway. Importantly, these two dendritic regions are differentially affected in TGNE mice, making them crucial components to study in order to better understand the functional consequences of the observed deficits. We conducted simulations with low-frequency (40 Hz; Supplementary Fig. 8a and c) and high-frequency (100 Hz; Supplementary Figs. 6d, 8b, and c) inputs applied to each virtual neuronal tree of both WT and TG models ($n = 71$), and examined their output firing patterns. When subjected to 40 Hz inputs spanning the complete dendritic tree encompassing the *stratum radiatum* and *stratum lacunosum*, TGNE neurons exhibited a significantly lower success rate of evoked spikes (82%) compared to WTNE neurons (100%) (Supplementary Fig. 8a). Consequently, the firing rate of TGNE neurons, averaged across all dendritic trees, was reduced (Supplementary Fig. 6c; output firing rate TGNE (2mo) vs. WTNE (2mo), $P < 0.05$), while both TGNE (32 Hz) and WTNE (40 Hz) models displayed low gamma oscillations.

In our simulations, when we applied high-frequency inputs (100 Hz) to the complete dendritic tree (*stratum radiatum* and *stratum lacunosum*) in WTNE neurons, we observed the expected success rate of evoked spikes associated with 100 Hz stimulation (Combe et al. 2018) (51%; Supplementary Fig. 8b), accompanied by an output firing rate indicative of high gamma oscillations (51 Hz). However, in the case of TGNE neurons, simulations with 100 Hz inputs revealed a significantly lower success rate of evoked spikes (39%) compared to WTNE neurons (Supplementary Fig. 8b and 7b). Consequently, the reduced success rate of evoked spikes in TGNE neurons resulted in a decreased output firing rate (39 Hz) in 2-month-old TG mice, which did not reach the high $\gamma$ frequency range (Supplementary Fig. 6c). Furthermore, when we examined the membrane potential (mV) in the multicompartmental simulations of representative dendritic trees spanning the *stratum radiatum* and *stratum lacunosum* regions, TGNE neurons failed to reach depolarization (Supplementary Fig. 6b). Additional details and results pertaining to the simulations conducted on *stratum radiatum* alone can be found in the Supplementary Text and Supplementary Figs. 6–8, where it is observed that TGNE neurons responded in the $\beta$ frequency range.

EE had a profound impact on the success rate of evoked spikes and the output firing, resulting in both TGEE and WTEE neurons achieving high $\gamma$ output frequencies (≥50 Hz; see Supplementary Fig. 6c). The comparison between TGEE and TGNE neurons revealed statistically significant differences in the input–output frequency upon 40 Hzinput ($P < 0.05$; Supplementary Fig. 6c) and 100 Hz input ($P < 0.05$; Supplementary Fig. 8a). Additionally, when examining the success rate of evoked spikes upon 40 Hz stimulation in both *stratum radiatum* and *stratum lacunosum*, the linear mixed effects treatment effect for 2mo groups indicated significant differences. Moreover, a significant difference was observed between TGEE and TGNE neurons ($P = 0.01$; Supplementary Fig. 8b) when 100 Hz stimulation was applied to both *stratum radiatum* and *stratum lacunosum*, as determined by the linear mixed effects treatment effect for 2mo groups. However, it should be noted that when only *stratum radiatum* was stimulated with 100 Hz, TGEE neurons were unable to surpass the $\beta$ threshold in firing activity (see Supplementary Text).

## Deficits in network activity of young TG CA1 neurons are rescued by environmental enrichment

We then examined whether the alterations in output firing, influenced by both genotype and EE, could impact the synchronized activity of CA1 neurons. To investigate this, we conducted simulations involving simultaneous inputs at 100 Hz, which mimicked the effects of tetanic stimulation, on a comprehensive population of reconstructed neurons. The number of neurons and animals included in the simulations were as follows: WTNE (2mo) = 18/4, TGNE (2mo) = 19/4, WTEE (2mo) = 19/4, TGEE (2mo) = 15/3. The average activity of these neurons was then measured. For these simulations, we focused on the combined input from the *stratum radiatum* and *stratum lacunosum*. To create a more realistic scenario, we incorporated inhibitory feedback into the model to explore the population-level effects of the stimulation. This inclusion allowed us to account for the observed over-inhibition in TGNE neurons and its subsequent recovery following EE (as depicted in Fig. 2c and d; for a detailed description of the methodology, please refer to the Methods section).

For all the simulations, we carefully selected the proportion of inhibitory synapses based on the measured VGLUT1/VGAT ratio in each experimental group, and accounting for observed proportions of inhibitory versus excitatory synapses in CA1 neurons (Megias et al. 2001). Additionally, we made adjustments to the proportion of active excitatory synapses in WTNE neurons, setting it at 7.5%. This adjustment aimed to replicate the physiological average firing rate of a single neuron when subjected to 100 Hz stimulation of Schaffer collaterals, considering the presence of inhibitory feedback at 20 Hz (Milstein et al. 2015). To account for potential variations in mature spine density among the experimental groups, we made further adaptations. Specifically, we adjusted the density of excitatory synapses in TG and EE-treated neurons by multiplying it with the ratio of mature spines to WTNE neurons. By incorporating this adjustment, we aimed to incorporate the impact of changes in mature spine density on the excitatory synapse distribution within the different groups.

We observed a notable decrease in the activity of the TGNE neuronal population compared to WTNE neurons (Fig. 3a, d, and e). The statistical analysis, using a two-way ANOVA, revealed a significant genotype effect, with TGNE neurons exhibiting significantly reduced activity compared to WTNE neurons ($P = 5e{-}11$). Given that over-inhibition is recognized as a characteristic feature of DS pathology, we aimed to discern the specific impact of TGNE over-inhibition. To isolate this effect, we simulated a "healthy" neuronal morphology, resembling that of WTNE neurons, but with TGNE inhibition (TGNE-Inh). Interestingly, this manipulation resulted in a 32% reduction in activity, indicating that over-inhibition alone cannot fully account for the observed decrease in network response in TGNE neurons (see Fig. 3b, d, and e).

Considering our hypothesis that alterations in neuronal architecture may also contribute to the suboptimal network response, we further simulated "normalized inhibition" conditions in TGNE neurons. This involved introducing the inhibitory feedback proportional to the VGAT puncta observed in WTNE neurons, thereby isolating the impact of neuron morphology. Under these "normalized inhibition" conditions, the TGNE neuron population already exhibited a 44% reduction in the power of averaged activity during 100 Hz stimulation, indicating that morphological changes play a significant role in the reduced network activity (see Fig. 3c, d, and e).

We then investigated the impact of EE on network activity, considering its strong potential to address both morphological and excitation-inhibition balance deficits in TG mice. During 100 Hz stimulation, we observed a significant increase of 42% in the averaged activity of TGEE neurons compared to TGNE neurons (refer to Fig. 3a, d, and e). The statistical analysis revealed a significant

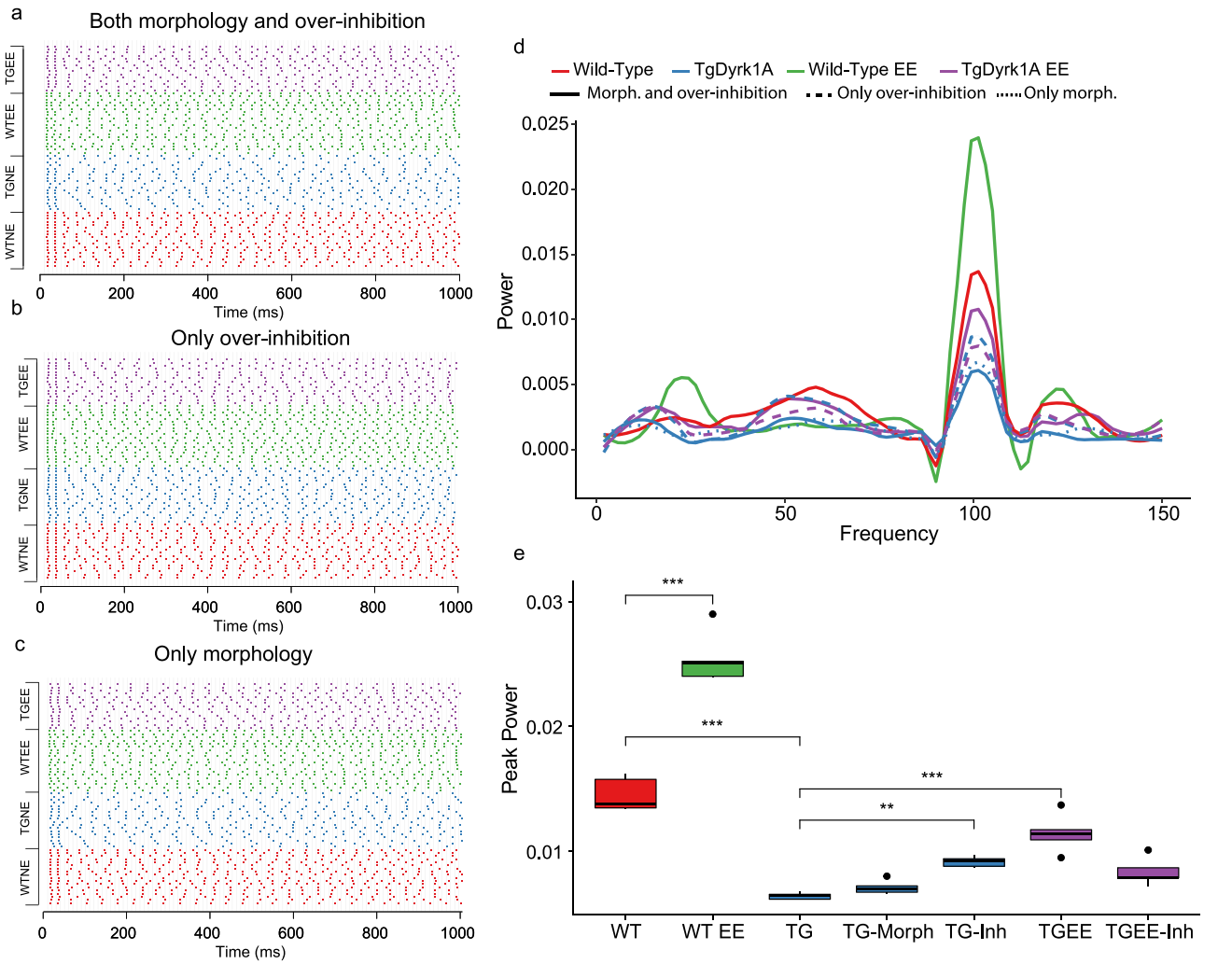


**Fig. 3.** Deficits in network activity of TG CA1 neurons are rescued by EE. Multicompartmental models were generated for 2mo WT and TG neurons with a number of inhibitory synapses based on proportions known in WT CA1 neurons. a–c) Spike raster plot of the simulated activity of CA1 neurons of 2mo WTNE, TGNE WTEE, and TGEE. In a, b, and c, each cell was stimulated with a 100 Hz input and with an inhibitory feedback loop. a) Models were generated with TGNE and WTNE (2mo) morphologies for EE and NE groups and we modeled the number of inhibitory synapses based on measured VGLUT1/VGAT ratio for 2mo TG and WT populations. Note the reduced firing in TG (2mo) neurons upon 100 Hz stimulation that is improved upon EE. b) In this case, models were generated with only WTNE (2mo) morphologies for EE and NE groups and we modeled the number of inhibitory synapses based on measured VGLUT1/VGAT ratio for 2mo TG and WT populations. c) Models were generated for 2mo WT and TG neuron morphologies with a number of inhibitory synapses based on measured VGLUT1/VGAT ratio. d) Power spectra of spiking activity obtained averaged over 10 simulation repetitions for WTNE (2mo) and TGNE (2mo). Dashed lines show the results of simulations accounting only for over inhibition (TG-Inh are WT morphologies with TG inhibition; TGEE-Inh are TG morphologies with TGEE inhibition; corresponding to the raster plot in b) and solid lines represent simulations accounting for both morphological features and over inhibition (corresponding to the raster plot in a). e) Peak power at 100 Hz for each of the neuron populations presented as boxplots. Two-way ANOVA, $^{**}P < 0.01$, $^{***}P < 0.001$. Number of neurons/animals: WTNE (2mo) = 18/4; TGNE (2mo) = 19/4; WTEE (2mo) = 19/4; TGEE (2mo) = 15/3.

treatment effect, with TGEE neurons displaying a significantly higher activity compared to TGNE neurons ($P = 5e{-}6$). However, when we exclusively simulated the rescue of over-inhibition, TGEE neurons only exhibited a modest 14% increase (refer to Fig. 3b). This finding further supports the notion that neuronal morphology has a stronger impact on the response of the neuronal population, as corroborated by spectral analysis (Fig. 3d and e, where the dashed purple line represents TG morphology with TGEE over-inhibition; TGEE-Inh vs. TGNE, N.S). On the other hand, in line with our hypothesis, the morphological changes observed in WT neurons following EE treatment led to a substantial 41% increase in power (Fig. 3a, d, and e).

In summary, the reduced network activity in TG neurons can be primarily attributed to deficits in neuronal architecture, with over-inhibition playing a lesser role. Moreover, the effects of EE on neuronal morphology are the main contributing factor to the improvement in network activity.

## Effects of EE on cognitive performance, levels of DYRK1A kinase activity, dendritic complexity, and spine morphology are lost after EE discontinuation (EEdis) in TG mice

The improvement in recognition memory observed in TGEE (2mo) mice following EE was not sustained 4 months after discontinuation of EE (EEdis) in TG mice at the age of 6 months. Specifically, TGEEdis (6mo) mice exhibited impaired object discrimination compared to TGEE (2mo) mice (Fig. 4a). The statistical analysis using a three-way ANOVA indicated a significant discontinuation effect, with TGEEdis (6mo) mice performing worse than TGEE (2mo) mice. It is worth noting that the EE conditions did not

enhance recognition memory in WTEE (2mo) mice. Consequently, when we evaluated the novel object recognition test at 6 months of age after EE discontinuation (WTEEdis; 6mo), WTEE mice performed similarly to the WTNE (6mo) mice, indicating no significant effect of EE discontinuation on their performance. Furthermore, the normalization of DYRK1A kinase activity achieved through EE was also reversed in 6-month-old TG mice following EEdis. Their DYRK1A kinase activity levels returned to increased levels observed in non-EE conditions (Fig. 4b). The respective values for DYRK1A kinase activity were as follows: WTNE (6mo) = 1.00 ± 0.12, TGNE (6mo) = 1.69 ± 0.21, WTEEdis (6mo) = 1.04 ± 0.24, TGEEdis (6mo) = 1.68 ± 0.14. Importantly, neither the object discrimination performance nor the DYRK1A kinase activity results were influenced by any age-related effects, as demonstrated by the statistical analysis (refer to Supplementary Fig. 9a and b; three-way ANOVA, age effect not statistically significant).

The width of the apical CA1 region was found to be smaller in both 2-month-old (2mo) and 6-month-old (6mo) TGNE mice compared to WTNE mice (Supplementary Fig. 3a and b). Statistical analysis using linear mixed effects models revealed a significant genotype effect for the NE groups, indicating that TGNE mice had a reduced width compared to WTNE mice. Specifically, TGNE-2mo mice showed a significant decrease in width compared to WTNE-2mo mice. This reduction in width was primarily attributed to a specific decrease in the width of the *stratum radiatum* (Supplementary Fig. 3c). The linear mixed effects analysis revealed a significant genotype effect for *stratum radiatum* width, indicating that both TGNE-2mo and TGNE-6mo mice had a significantly smaller *stratum radiatum* width compared to their respective WTNE.

The rescuing effect of EE on the width of CA1 *stratum radiatum* in TGEE mice was no longer significant upon discontinuation of EE (Supplementary Fig. 3a–c). The linear mixed effects analysis revealed a nonsignificant interaction between genotype and treatment for the EEdis (6mo) groups, as well as a nonsignificant age effect. However, there was a significant genotype effect for the EEdis (6mo) groups.

In addition, dendritic complexity, as assessed by Sholl analysis, was reduced to NE levels in both WT and TG mice (Fig. 4c and e). The statistical analysis indicated a significant effect of treatment discontinuation, with *P*-values below 0.05 observed between 100 and 320 $\mu$m, and significant differences between WTEE (2mo) and WTEEdis (6mo) mice at specific ranges (between 160 and 180 $\mu$m, and 240 and 280 $\mu$m). Similarly, the dorso-ventral span of apical dendrites showed a reduction to NE levels in TGEE mice upon discontinuation (refer to Fig. 4d). The linear mixed effects analysis revealed a significant discontinuation effect, but no significant difference was observed between TGEEdis and TGNE mice at 6 month of age.

To rule out the influence of age on the effects of EE discontinuation, a comparison was made between 6-month-old WTNE and TGNE mice (WTNE-6mo and TGNE-6mo) and their younger 2mo counterparts (WTNE-2mo and TGNE-2mo). No significant age effects were found for *stratum radiatum* width, dorso-ventral span, or Sholl analysis in either WTNE or TGNE mice (Supplementary Figs. 3c, 4a, and c). Overall, these results indicate that the dendritic remodeling effect of EE in the hippocampal CA1 region of TG mice is completely lost upon discontinuation of EE.

Additionally, the discontinuation of EE resulted in the loss of the treatment effect on spine density in TGEEdis mice, particularly affecting the density of mature (type C) spines (Fig. 4f–h). Statistical analysis using linear mixed effects models showed a significant discontinuation effect on type C spines, indicating that TGEEdis mice had a decrease in type C spine density compared to TGEE mice (TGEEdis vs. TGEE, $P = 0.05$). Importantly, these findings were not influenced by age, as all spine classes remained unchanged with age in TGNE mice (Supplementary Fig. 4i and j). However, we observed a significant reduction in mushroom-like type C spines in 6mo WT mice compared to 2mo WT mice (Fig. 4m and n), which may explain the detected effect of EEdis in WT mice (refer to Figs. 4l and 5m). It is worth noting that no age-related differences in the total density of dendritic spines of CA1 pyramidal neurons located in the *stratum radiatum* layer were observed in the NE groups (refer to Supplementary Fig. 4c).

## EE-induced improvement of synaptic plasticity is lost upon EE discontinuation in TgDyrk1A mice

Upon discontinuation, the EE effects on paired-pulse facilitation (Fig. 5a), and on LTP were lost in TGEE-6mo (Fig. 5b). This was not due to an age effect on the LTP response (Supplementary Fig. 10a). We detected a significant genotype-related reduction in LTP for both 2mo and 6mo TGNE mice (Supplementary Fig. 10a). In addition, the excitation-inhibition imbalance showed a significant genotype effect in NE groups at both 2mo and 6mo mice (Supplementary Fig. 10b), showing a nonsignificant trend to decreased VGLUT1/VGAT ratio after EEdis (Supplementary Fig. 10b). Those results were also not dependent on age.

## EE effects on the connectivity repertoire and input–output frequency relationship were lost after treatment discontinuation in both TG and WT mice

When considering only dendritic tree span and complexity, the increase in connectivity repertoire observed with EE in both WT and TG mice was no longer present after discontinuation of EE (Supplementary Fig. 5a). Linear mixed effects models showed a significant discontinuation effect on connectivity repertoire, with TGEE (2mo) mice exhibiting higher connectivity repertoire compared to TGEEdis (6mo) mice. Similarly, when analyzing mature spine densities, the beneficial effect of EE was lost (Supplementary Fig. 5b). Linear mixed effects models revealed a significant discontinuation effect on mature spine densities, indicating that both WTEEdis (6mo) and TGEEdis (6mo) neurons had similar connectivity repertoire levels as their NE 6mo counterparts (NE 6mo; refer to Supplementary Fig. 5b). Moreover, the genotype-dependent reduction in connectivity repertoire observed in TGNE mice at 2 months of age persisted at 6 months of age. Importantly, connectivity repertoire did not significantly change with age in either genotype in the NE groups (refer to Supplementary Fig. 5b).

Upon in silico low-frequency 40 Hz and high-frequency 100 Hz stimulation of the entire dendritic tree, neurons in the EEdis (6mo) group exhibited a significant decrease in their success spiking rate and firing rate compared to the enriched EE (2mo) group in both genotypes (Supplementary Fig. 8a). Linear mixed effects models showed a significant discontinuation effect on success spiking rate, with TGEEdis (6mo) mice displaying lower success spiking rates compared to TGEE (2mo) mice. Similarly, a significant discontinuation effect was observed for firing rate, indicating that both WTEEdis (6mo) and TGEEdis (6mo) neurons had lower firing rates compared to their enriched counterparts, WTEE (2mo) and TGEE (2mo), respectively. Interestingly, neither WTEEdis nor TGEEdis neurons were able to reach high $\gamma$ oscillation states (Supplementary Fig. 11e). These effects were not influenced by age-related differences in success rate or output firing, as there were no significant differences between WTNE-6mo and TGNE-6mo compared to their respective 2-month-old

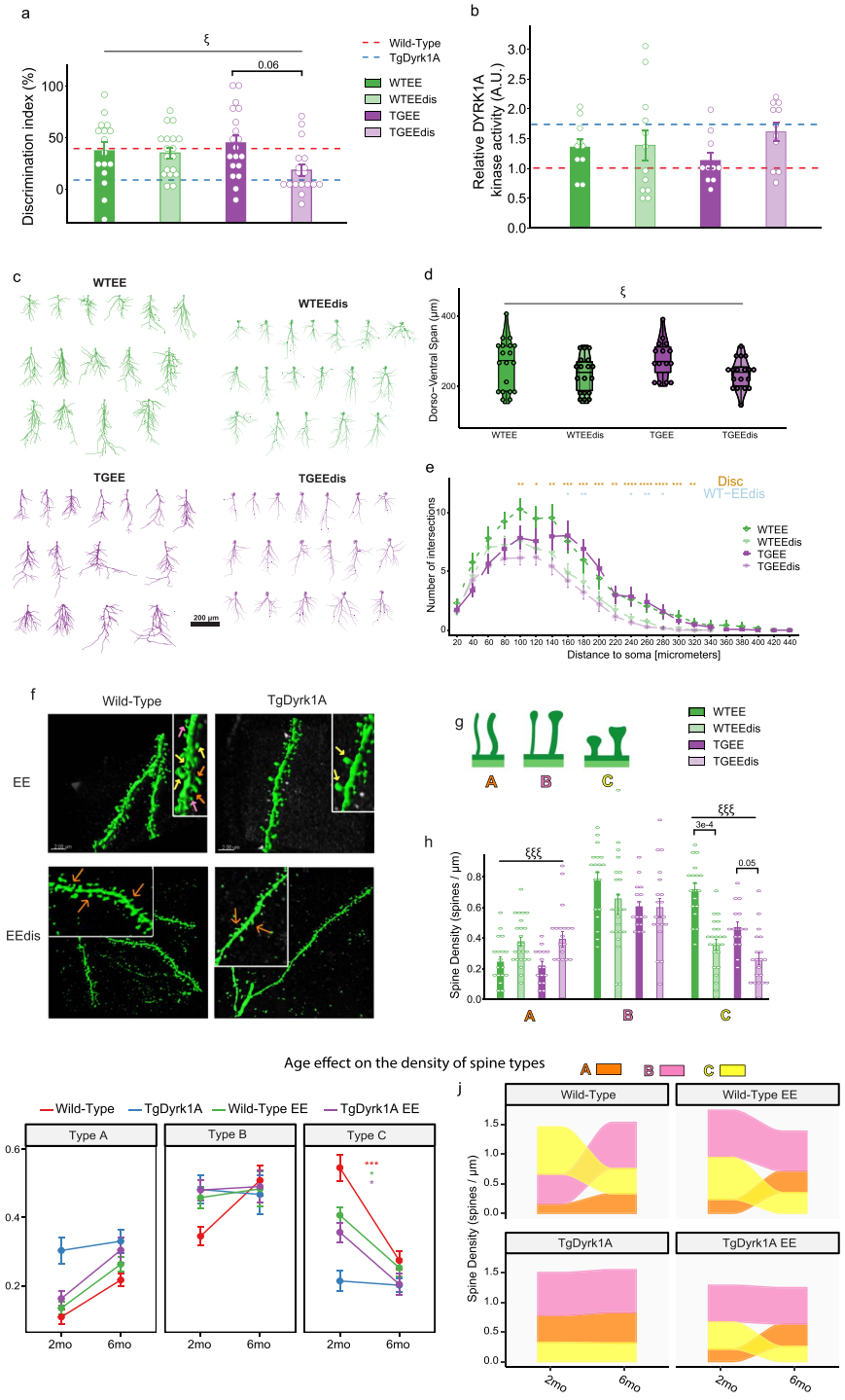


**Fig. 4.** Long-term effects on cognitive performance, levels of DYRK1A kinase activity, dendritic complexity and spine morphology are lost after EE discontinuation in TgDyrk1A mice. a) Discrimination index of the NOR paradigm in WT and TG mice reared on EE and reared on EE followed by 4 months under NE conditions (EEdis): WTEE (2mo) = 16; TGEE (2mo) = 19, WTEEdis (6mo) = 18; TGEEdis (6mo) = 18. Linear mixed effects, treatment discontinuation effect ξ $P < 0.05$. b) Relative DYRK1A kinase activity in the hippocampus. WTEE (2mo) = 12; TGEE (2mo) = 11; WTEEdis (6mo) = 12; TGEEdis (6mo) = 12. Data are expressed as mean ± SEM. Three-way ANOVA. Colored dashed lines indicate reference mean values for 2mo WTNE and TGNE groups. c) 2D projection of all reconstructed apical dendritic trees (coronal plane) in WT and TG, upon EE (2mo) and after EEdis (6mo). Scale bar = 200 $\mu$m. d) Length of CA1 apical dendritic trees along the dorso-ventral axis. Data are presented as an overlay of dotplots, boxplots and violin plots. WTEE (2mo) = 19/4, TGEE (2mo) =15/3; WTEEdis (6mo) = 18/3; TGEEdis (6mo) = 18/4. Linear mixed effects, treatment discontinuation effect ξ $P < 0.05$. e) Sholl analysis. Lines indicate mean ± SEM. Linear mixed effects, *$P < 0.05$, **$P < 0.01$. f) Representative confocal images showing CA1 apical dendritic spines in WT and TG mice under EE (2mo) or discontinued EE (6mo) conditions. Scale bar = 200 $\mu$m. Right upper insert corresponds to a higher magnification. Orange, pink and white arrows denote type A, type B and type C spines, respectively. g) Illustration of the morphological categories used to classify spines. h) Density of each spine type. Data are presented as mean ± SEM. Linear mixed effects, treatment discontinuation effect ξξξ $P < 0.001$. i) Age-related changes in the percentage of spine types (A, B, C). Data are presented as mean ± SEM. Data are paired along time for each experimental group (colored lines). Linear mixed effects, *$P < 0.05$, ***$P < 0.001$. j) Sankey plots of the density of each spine type for WT and TG mice both NE and after EE treatment (2 and 6 mo) and its discontinuation (6mo). Orange, pink, and yellow represent spines of types A, B, and C, respectively. The width of each band indicates spine density in number of spines per micrometer. (f–j) Number of dendrite segments/neurons reconstructed/animals analyzed: WTNE-2mo 19/19/4; TGNE-2mo 16/12/4; WTEE (2mo) = 19/19/4, TGEE (2mo) = 16/9/4; WTNE-6mo 20/20/4; TGNE-6mo 19/19/5; WTEEdis (6mo) = 18/18/3; TGEEdis (6mo) = 18/18/6).

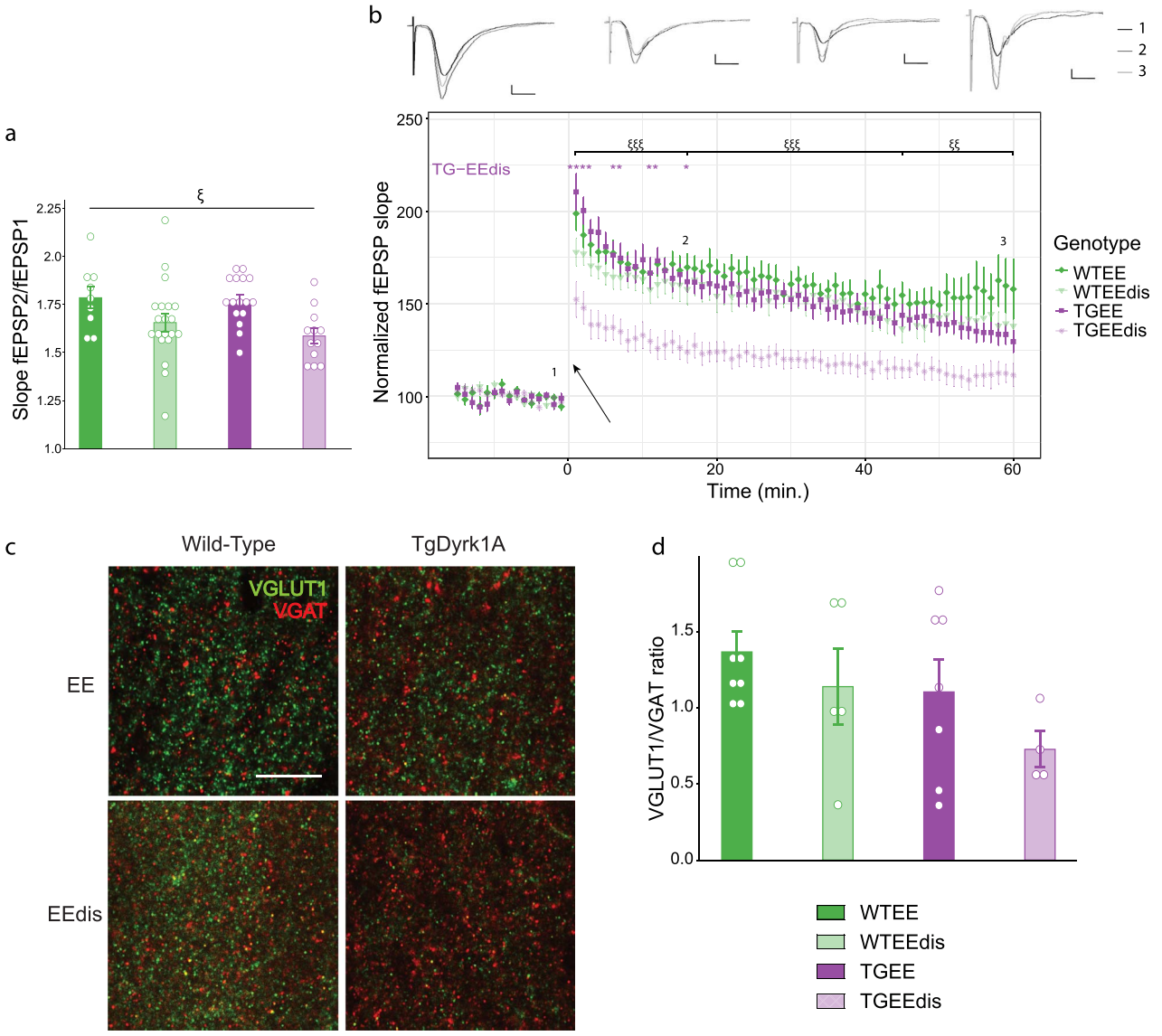


**Fig. 5.** Changes in synaptic plasticity are lost in TgDyrk1A mice after EE discontinuation. a) Paired pulse facilitation (fEPSP2/fEPSP1) in the hippocampus with an inter-stimulus interval of 50 ms of WT and TG mice reared under EE conditions for 1 month (2mo) or after EE discontinuation (EEdis, 6mo). Slices/animals: WTEE (2mo) = 9/5; TGEE (2mo) = 16/5; WTEEdis (6mo) = 20/7; TGEEdis (6mo) = 12/5. Three-way ANOVA treatment discontinuation effect $\xi$ $P < 0.05$. b) LTP in CA1 induced by TBS in CA3. Upper panel: representation of the mean of 5 responses to stimulation at time 1 (−5 min), 2 (15 min), and 3 (60 min). Vertical bar represents 500 $\mu$V, horizontal bar represents 5 ms. Lower panel: normalized fEPSP slope before and after TBS. Black arrow represents the time of TBS application ($t = 0$). Three-way ANOVA; $\xi\xi$ $P < 0.01$, $\xi\xi\xi$ $P < 0.001$. c) Representative confocal images showing VGLUT1+ and VGAT+ punctae in the CA1 *stratum radiatum* hippocampal subfield. Scale bar = 10 $\mu$m. d) Histogram showing the ratio between VGLUT1+ and VGAT+ punctae. WTEE (2mo) $n = 8$; TGEE (2mo) $n = 7$; WTEEdis (6mo) $n = 5$; TGEEdis (6mo) $n = 4$. Data are represented as mean + SEM.

counterparts, WTNE-2mo and TGNE-2mo, in any of these measures (WTNE-6mo achieved high $\gamma$ oscillations similar to WTNE-2mo, while TGNE-6mo did not, similar to TGNE-2mo; Supplementary Fig. 7a and b). When simulating inputs specifically on the *stratum radiatum* region, both WT and TG neurons showed a slight reduction in output firing rate following EE discontinuation. However, the effects were not as pronounced as when stimulating the entire dendritic tree (see Supplementary Text and Supplementary Fig. 11).

In summary, our findings indicate that the positive impact of EE on the response to 100 Hz inputs in the entire dendritic tree is lost in TGEEdis neurons following discontinuation. As a result, these neurons remain unable to reach high gamma ($\gamma$) frequencies. This loss can be attributed to the diminished effects of EE on dendritic tree complexity, which, coupled with decreased mature spine density, leads to reduced integration of coincident inputs in both WTEEdis and TGEEdis neurons.

## EE effects on the activity of CA1 neuronal populations are lost after treatment discontinuation

When simulating 100 Hz stimulation on the CA1 neuronal population, taking into account the inhibition phenotype, we observed a significant reduction in network activity in both WTEEdis (6mo) and TGEEdis (6mo) compared to the enriched conditions (2mo) (Fig. 6a). The power of the network activity was reduced by 72%, indicating a marked decrease in network responsiveness (Fig. 6b and c).

The effect of EE discontinuation can be partly attributed to an age-dependent reduction in network activity observed in both WT

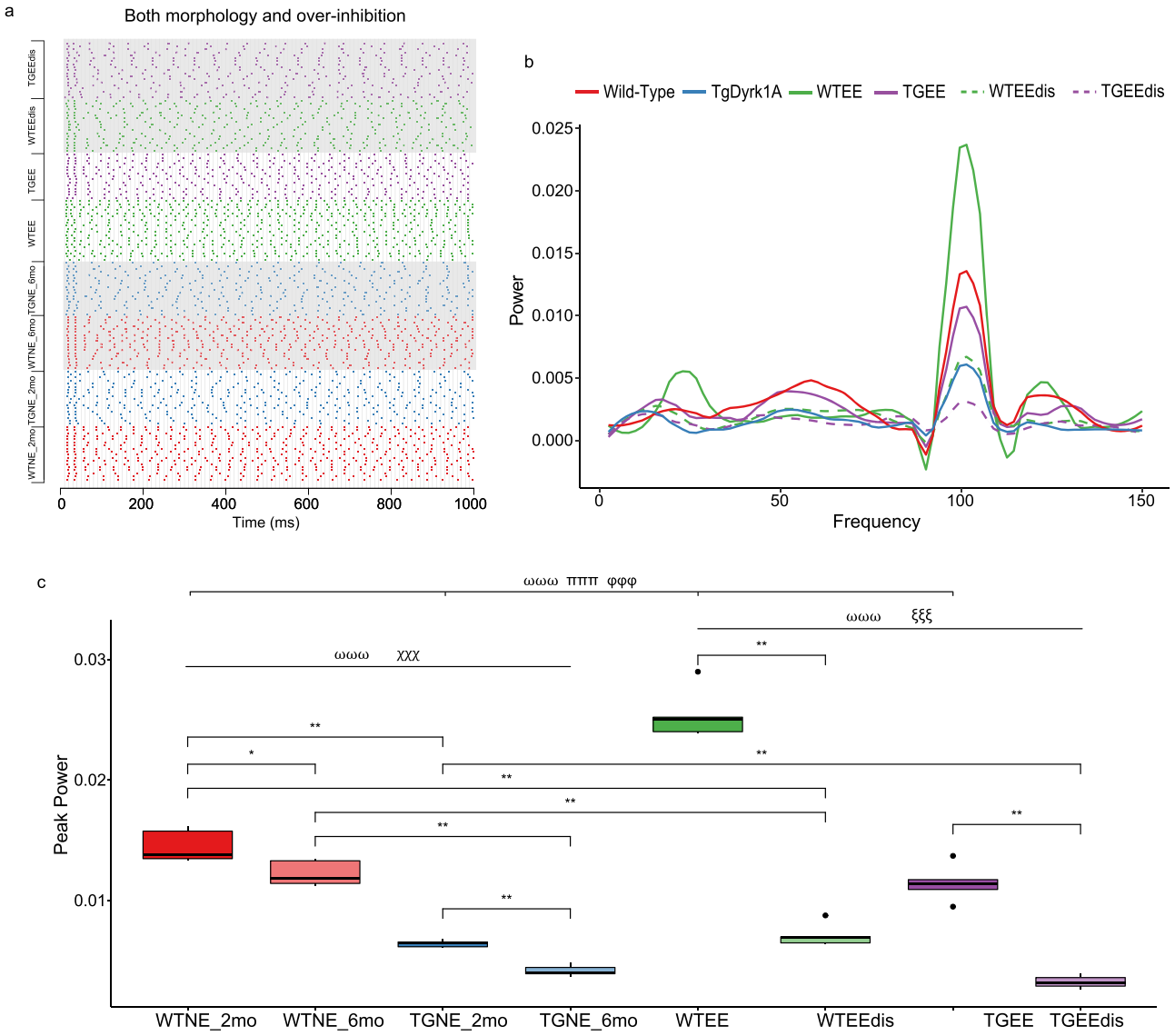


**Fig. 6.** EE effects on averaged activity of TgDyrk1A CA1 neurons are lost after treatment discontinuation. a) Spike raster plot of the simulated activity of CA1 neurons of WTNE, TGNE WTEE, and TGEE, taking into account both. Note the reduced firing in both WT and TG NE_6mo neurons upon 100 Hz stimulation that is more marked upon Eedis in WTEEdis and TGEEdis. Raster plots overlayed by gray blocks indicate 6mo and EEdis groups. b) Power spectra of spiking activity obtained upon simulation of 100 Hz input frequency and averaged over 10 simulation repetitions for WT and TG NE, EE and EEdis groups. Dashed lines show the results of simulations accounting for EEdis. c) Peak power at 100 Hz for each of the neuron populations presented as boxplots. Number of neurons/animals: WTNE = 18/5; TGNE = 18/5; WTEE = 18/3; TGEE = 18/4. Three-way ANOVA, genotype effect $\omega\omega\omega$ $P < 0.001$; treatment effect $\pi\pi\pi$ $P < 0.001$; genotype × treatment interaction $\varphi\varphi\varphi$ $P < 0.001$; treatment discontinuation effect $\xi\xi\xi$ $P < 0.001$; age effect $\chi\chi\chi$ $P < 0.001$. *$P < 0.05$, **$P < 0.01$.

(14%) and TG (39%) groups (Fig. 6c). Furthermore, we discovered a detrimental effect of EE discontinuation, as WTEEdis mice exhibited significantly reduced neuronal population activity compared to WTNE_6mo mice (42%).

## Discussion

The present study sought to investigate the role of architectural features in shaping alterations of rhythmic activity at the local neuronal population level. Our study utilized in silico modeling techniques to explore this complex phenomenon, with a particular focus on Dyrk1A overexpression, a DS candidate gene. It has long been speculated that these abnormalities could be critical markers of cognitive impairment, leading researchers to explore therapeutic approaches that target neural plasticity in the hopes of improving cognitive function (Dierssen and Ramakers 2006). Studies have revealed that EE interventions can effectively rescue microstructural phenotypes associated with neuronal abnormalities in DS mouse models (Martínez-Cué et al. 2002; Dierssen et al. 2003; Mahoney et al. 2006; Begenisic et al. 2011). Our research centered around a mouse model that overexpresses Dyrk1A, one of the most relevant candidate genes associated with DS. We wanted to better understand the functional implications of dendritic alterations and how they can be rescued by environmental intervention.

Our behavioral experiments recapitulated the impaired performance previously reported in the Novel Object Recognition (De Toma et al. 2019). TG mice showed significantly reduced object discrimination, as described in other DS (Fernandez and Garner 2008) and transgenic *Dyrk1A* models (Guedj et al. 2009).

We also identified structural and functional alterations in the hippocampus of TG mice mirroring the hippocampal phenotypes observed in DS (Martínez-Cué et al. 2002; Dierssen et al. 2003; Mahoney et al. 2006; Begenisic et al. 2011; Martinez de Lagran et al. 2012). Additionally, we detected an imbalance between excitatory and inhibitory neurotransmission, biased toward inhibition, due to a reduced number of VGLUT1 puncta (excitatory vesicles) (Kurt et al. 2004; Souchet et al. 2014), along with impaired LTP in CA3-CA1. Furthermore, our investigation into the dendritic arbor architecture and spine density in the CA1 neurons of the transgenic mice revealed intriguing differences in structural organization of CA1 subfield. We observed decreased apical dendritic tree span and complexity, alongside a more immature spine phenotype. These changes likely reduce the number of afferent inputs and limit the potential input combinations, as highlighted by our connectivity repertoire analysis. This finding is crucial, as dendritic arbor architecture plays a vital role in local computation processes, specifically in the integration of pre- and post-synaptic events (Larkum et al. 2009; Branco et al. 2010; Branco and Häusser 2011; Emoto 2012; Kim et al. 2012). Our morphological analysis and modeling focused on postsynaptic features. However, the reduction in paired pulse facilitation we observed suggests presynaptic alterations co-exist with postsynaptic ones, contributing to the phenotype. It is reasonable to assume that endocytosis will be affected by DYRK1A overexpression, as many of its substrates are involved in endocytosis (Bonnycastle et al. 2021). The modeling in this article should be interpreted as a conservative estimate of reduced postsynaptic integration only dependent on the number of synapses, but individual synapses are equal in both WT and TG neurons. Reduced presynaptic release of neurotransmitters, or abnormal uptake of those in postsynaptic sites would further exacerbate the impact we observed in our model. Thus, further work is needed to model synaptic mechanism alterations in TG, disentangling pre- and postsynaptic perturbations, and exploring the contribution of those on single neuron dynamics and LTP.

One of the intriguing findings of our study is the layer-specific nature of the dendritic alterations observed in TG CA1 subfield, with a prominent reduction in dendritic width in the *stratum radiatum*. This led us to delve deeper into understanding how these deficits could impact the network dynamics in TG CA1. Using multicompartmental models, we examined the input–output relationship of firing frequencies in individual CA1 pyramidal neurons as a reduced connectivity repertoire may affect neuronal signal integration (Chklovskii et al. 2002). Specifically, we simulated scenarios involving the complete dendritic tree spanning both the *stratum radiatum* and *stratum lacunosum-moleculare*, as well as simulations focusing solely on the *stratum radiatum* region, where the reduced dendritic width was predominantly observed. In normal WT neurons, it is expected that selective stimulation of the Schaffer collateral pathway in the *stratum radiatum* alone, even at high frequencies, would result in low gamma ($\gamma$) frequency output firing, a property known as frequency selectivity (Combe et al. 2018). Instead, combined input from the Schaffer collateral and the perforant path to both *stratum radiatum* and *stratum lacunosum* can lead to higher frequency output firing through coincidence detection (Schaefer et al. 2003; Jarsky et al. 2005). This frequency selectivity is crucial for CA1 cells to synchronize selectively with either the CA3 region at low $\gamma$ or the entorhinal cortex at high $\gamma$ during different cognitive tasks, such as spatial exploration or object-place pairing (Colgin et al. 2009; Zheng et al. 2016). In fact, it has been shown that prospective coding occurs when CA1 cells mainly fire at low $\gamma$ during spatial exploration tasks (Bieri et al. 2014). To assess whether frequency selectivity (e.g. the fact that CA1 selectively "listen" to CA3 at slow gamma) could be impaired in TG CA1 neurons, taking into account the reduced synaptic connectivity resulting from the observed dendritic alterations, we conducted simulations involving Schaffer collateral inputs affecting only the *stratum radiatum* region or synapses receiving inputs from both the *stratum radiatum* and *stratum lacunosum* regions. The results were striking: when the model received only *stratum radiatum* inputs, TG neurons were unable to reach low $\gamma$ frequencies. Furthermore, when we stimulated both *stratum radiatum* and *stratum lacunosum*, TG neurons failed to reach high $\gamma$ frequencies. These findings suggest that the ability to switch between low and high $\gamma$ coupling between CA1 and the entorhinal cortex may be compromised in TG mice. Interestingly, this aligns with previous research by Munn et al., which demonstrated that Ts65Dn CA1 pyramidal cells exhibit a preference for slow gamma phase-locking over fast gamma (Munn et al. 2022). Consequently, this perturbed $\gamma$ coupling could potentially impair the ability to distinguish familiar from novel environments, which has been implicated in various cognitive processes (Colgin et al. 2009; Zheng et al. 2016). Our computational modeling approach, incorporating the observed dendritic alterations, provides valuable insights into the potential functional consequences at the network level. The findings suggest that the dendritic deficits in TG CA1 neurons may disrupt the delicate balance of gamma frequency coupling, which is crucial for information processing and cognitive functions.

The reduced ability of single neurons to reach high $\gamma$ suggests that architectural features are relevant to produce alterations of rhythmic activity at the local neuronal population level. Previous research has demonstrated a decrease in high $\gamma$ activity within cortical and hippocampal local networks in TgDyrk1A and trisomic models, (Ruiz-Mejias et al. 2016; Alemany-González et al. 2020). This decline has primarily been attributed to excessive GABA-mediated neurotransmission (Reynolds and Warner 1988; Risser et al. 1997). However, the potential contribution of architectural features had not been thoroughly investigated. Therefore, our study aimed to shed light on this aspect. To explore the impact of morphological alterations, we utilized multicompartmental models of traced neurons in a simulated CA1 neuronal population to test in silico their ability to fire synchronously at high $\gamma$. We stimulated these models with simultaneous input and incorporated recurrent local inhibitory feedback, including point inhibitory neurons that both inhibit pyramidal neurons and themselves. This approach allowed us to realistically simulate the inhibitory interactions within the neuronal network.

Our simulations yielded intriguing results. We observed that reduced spine density, as well as alterations in dendritic tree span and complexity, exerted a stronger influence on the ability of CA1 neurons to fire synchronously at high $\gamma$ frequencies compared to over-inhibition from local circuits. These findings suggest that architectural features play a significant role in shaping population activity rhythms. These results challenge the prevailing notion that excessive GABAergic transmission alone accounts for alterations in population activity rhythms in DS models. While excessive inhibition remains a contributing factor, our study highlights the importance of considering the intricate details of neuronal structure. The reduced ability of single neurons to reach high $\gamma$ frequencies implies that alterations in spine density, dendritic tree span, and complexity can disrupt the delicate balance of neural activity and impact population-level rhythmic activity.

The remarkable potential of EE in rescuing cognitive deficits, dendritic abnormalities, and synaptic plasticity alterations in DS

mouse models has been widely documented (Martínez-Cué et al. 2002; Dierssen et al. 2003; Mahoney et al. 2006; Begenisic et al. 2011). Previous studies have shown that EE can increase spine density and promote the stabilization of new synapses, thereby enhancing neural connectivity (Bednarek and Caroni 2011). Consistent with these findings, our study demonstrated that EE effectively increased mature spine density in TG mice, suggesting a stimulation of spine maturation and stabilization rather than de novo spinogenesis (Johansson and Belichenko 2002; Bindu et al. 2007; Beauquis et al. 2010). Moreover, although the increase in dendritic span and complexity with EE did not reach statistical significance, it nonetheless contributed to an overall improvement in the connectivity repertoire of the neuronal network. In addition to the positive effects on spine density and dendritic morphology, we observed a significant increase in the VGLUT1/VGAT ratio, indicating an enhanced excitatory-inhibitory balance. This finding is noteworthy, as previous work demonstrated that modulating inhibitory signaling can rescue cognitive impairment in DS mouse models (Fernandez et al. 2007). However, it is worth mentioning that GABAA $\alpha$5 subunit inverse agonist treatment, which aims to reduce inhibition, did not yield significant improvements in cognition in a recent clinical trial (RG1662; Hoffman-La Roche). Our simulation results align with this discrepancy, suggesting that simply correcting the excitation-inhibition balance may not be sufficient to rescue fast $\gamma$ activity. Based on our findings, it can be speculated that a more effective treatment for DS should not only target the reduction of inhibition but also promote the enhancement of dendritic architecture and spine maturation. Indeed, studies have reported that pentylenetetrazol, a GABAA antagonist, not only reduces inhibition but also increases mature spine density and dendritic morphology in rat CA1 neurons (Flores-Soto et al. 2021) and snails (Altrup and Speckmann 1988). In contrast, treatments that decrease dendritic arborization and impair spine maturation, such as GABAA $\alpha$5 subunit inverse agonist treatment in hippocampal neurons in vitro, may not be as effective (Giusi et al. 2009; Brady and Jacob 2015). Therefore, further research is warranted to elucidate the impact of GABAA antagonists on dendritic architecture, which may pave the way for improved pharmacotherapy for DS.

An important aspect of our study was to investigate the stability of the effects of EE upon discontinuation, which is a critical concern in early intervention strategies for DS (Mahoney et al. 2006; Bonnier 2008). The fear is that cognitive improvements achieved through intervention may not persist after the intervention is ceased, necessitating lifelong and costly interventions to maintain the positive effects. To address this issue, we examined previously EE-exposed animals after 4 months of EE discontinuation to assess the longevity of the phenotypic rescue.

Remarkably, we found that the rescuing effects of EE on dendritic structure, spine morphology, hippocampal CA1 synaptic plasticity, and short-term memory were lost in transgenic (TG) mice after discontinuation. This loss of effect was accompanied by the loss of the normalization of the excess DYRK1A kinase activity (Pons-Espinal et al. 2013), which had been previously rescued by 1 month of EE exposure in TG mice. These findings suggest that the overexpression of *Dyrk1A* may hinder the maintenance of activity-dependent neuronal plasticity improvements in DS pathology. To further understand the impact of EE discontinuation, we incorporated these observations into our computational model. We observed that TG neurons, after discontinuation of EE, exhibited firing frequencies comparable to their NE counterparts both at the single-cell and local population levels. While the effects of EE discontinuation in WT did not have a significant impact on object discrimination nor DYRK1A kinase activity, they showed a significant decrease in mature spine density and a nonsignificant decrease in VGLUT1/VGAT puncta ratio. The combination of those led to a significantly decreased $\gamma$ firing at the local population level. While LTP was not impaired in WT after EE discontinuation, further exploration is needed to confirm any potential impairment and its associated spine phenotype.

Both the novel-object recognition test and EE are closely linked to adult neurogenesis in the Dentate Gyrus (Kempermann et al. 1997; Jessberger et al. 2009). Our team previously reported adult neurogenesis alterations in this TG mouse model with reproducible behavioral outcomes consistent with our results (Pons-Espinal et al. 2013). Those, and the age-related attenuation of the treatment effect, could be partially explained by perturbed adult neurogenesis (Encinas et al. 2011). One exciting possibility is exploring the impact of adult neurogenesis on the storage capacity of DG, or the tri-synaptic circuit, from a modeling perspective. Such work could also help to better understand the role of adult neurogenesis and further dissect it from the contribution of CA1 in both memory formation and retrieval.

The present study has several limitations that warrant consideration. First, our investigation relied on in silico modeling, which may not fully capture the complexities of in vivo neuronal networks. Further studies using in vivo or in vitro approaches are necessary to validate and expand upon our findings. Second, our focus was limited to CA1 neuronal populations, and it remains to be determined whether similar findings can be observed in other brain regions or neuronal populations. Finally, the 4-month EE discontinuation period in our study may not fully capture the long-term consequences, and further investigations with longer follow-up periods are warranted.

In conclusion, our study provides compelling evidence that architectural features have a substantial impact on alterations in rhythmic activity at the local neuronal population level. We have demonstrated that reduced spine density, as well as alterations in dendritic tree span and complexity, exert a stronger influence than over-inhibition from local circuits on the ability of CA1 neurons to fire synchronously at high $\gamma$ frequencies. These findings highlight the need to consider the intricate interplay between architectural features and neurotransmission in DS and related conditions. We demonstrated that these impairments can be temporarily rescued through EE, which induces remodeling of distal dendrites in CA1 pyramidal cells and restores both mature spines and the excitation-inhibition balance.

We conclude that synaptic and structural neuronal defects in TG mice lead to impaired cognition by impairing hippocampal CA1 integration of CA3 and entorhinal cortex inputs and that excessive inhibition is only partially responsible for decreased local population oscillatory activity, suggesting that microarchitectural neuronal features are more relevant than previously thought. Further investigations are warranted to deepen our understanding of these complex mechanisms and potentially pave the way for novel therapeutic interventions.

## Acknowledgments

All confocal imaging was done in the CRG Advanced Light Microscopy Facility. We acknowledge the support from Gemma Comas for their help imaging the single neuron slice sections. We are grateful to Santiago Acosta for his help in generating the single neuron reconstructions, and Juan Luis Musoles for his help in the preprocessing of CA1 lower magnification image stacks.

## Author contributions

Linus Manubens-Gil (Formal analysis, Investigation, Software, Visualization, Writing—original draft, Writing—review & editing), Meritxell Pons-Espinal (Formal analysis, Investigation, Visualization, Writing—original draft, Writing—review & editing), Thomas Gener (Investigation, Writing—review & editing), Inmaculada Ballesteros-Yanez (Investigation, Writing—review & editing), María Martínez de Lagrán (Conceptualization, Writing—original draft, Writing—review & editing), and Mara Dierssen (Conceptualization, Funding acquisition, Project administration, Writing—original draft, Writing—review & editing)

## Lead contact

Further information and requests for resources and reagents should be directed to and will be fulfilled by the lead contact Prof. Mara Dierssen—mara.dierssen@crg.eu.

## Supplementary material

Supplementary material is available at *Cerebral Cortex* online.

## Funding

We acknowledge support of the Spanish Ministry of Economy and Competitiveness (MINECO), "Centro de Excelencia Severo Ochoa 2013-2017", SEV-2012-0208. The research leading to these results has received funding from MINECO (SAF2013-49129-C2-1-R; PID2022-141900OB-I00 and PID2019-110755RB-I00/AEI/10.13039/501100011033), H2020 SC1 Gene overdosage and comorbidities during the early lifetime in DS GO-DS21-848077, Jerôme Lejeune Foundation #2002, the NIH grant R01 EB028159 We acknowledge support of the Spanish Ministry of Science and Innovation to the EMBL partnership, the Centro de Excelencia Severo Ochoa ((CEX2020-001049-S, MCIN/AEI/10.13039/501100011033)) and the CERCA Programme/Generalitat de Catalunya. The CIBER of Rare Diseases is an initiative of the ISCIII.

*Conflict of interest statement:* The authors declare no competing interests.

## Data availability

Neuron reconstructions have been deposited at the NeuroMorpho.Org repository and at GitHub: https://github.com/lmanubens/EE_CA1/tree/main/data. Source data for all the analyses can be found at: https://github.com/lmanubens/EE_CA1/tree/main/shiny_app.

All original code for the Shiny app, statistical analysis and plotting has been deposited at GitHub and is publicly available as of the date of publication: https://github.com/lmanubens/EE_CA1/tree/main/shiny_app. Code for multicompartmental modeling can be found at: https://github.com/lmanubens/EE_CA1/tree/main/model. Any additional information required to reanalyze the data reported in this work paper is available from the corresponding authors upon request.

## References

Ahn K-J, Jeong HK, Choi H-S, Ryoo S-R, Kim YJ, Goo J-S, Choi S-Y, Han J-S, Ha I, Song W-J. DYRK1A BAC transgenic mice show altered synaptic plasticity with learning and memory defects. *Neurobiol Dis*. 2006:22:463–472.

Alemany-González M, Gener T, Nebot P, Vilademunt M, Dierssen M, Puig MV. Prefrontal-hippocampal functional connectivity encodes recognition memory and is impaired in intellectual disability. *Proc Natl Acad Sci U S A*. 2020:117:11788–11798.

Altafaj X, Dierssen M, Baamonde C, Martí E, Visa J, Guimerà J, Oset M, González JR, Flórez J, Fillat C, et al. Neurodevelopmental delay, motor abnormalities and cognitive deficits in transgenic mice overexpressing Dyrk1A (minibrain), a murine model of Down's syndrome. *Hum Mol Genet*. 2001:10:1915–1923.

Altrup U, Speckmann E-J. Epileptic discharges induced by pentylenetetrazol: changes of shape of dendrites. *Brain Res*. 1988:456:401–405.

Beauquis J, Roig P, Nicola AFD, Saravia F. Short-term environmental enrichment enhances adult neurogenesis, vascular network and dendritic complexity in the hippocampus of type 1 diabetic mice. *PLoS One*. 2010:5:e13993.

Bednarek E, Caroni P. $\beta$-Adducin is required for stable assembly of new synapses and improved memory upon environmental enrichment. *Neuron*. 2011:69:1132–1146.

Begenisic T, Spolidoro M, Braschi C, Baroncelli L, Milanese M, Pietra G, Fabbri ME, Bonanno G, Cioni G, Maffei L, et al. Environmental enrichment decreases GABAergic inhibition and improves cognitive abilities, synaptic plasticity, and visual functions in a mouse model of down syndrome. *Front Cell Neurosci*. 2011:5:29.

Beining M, Mongiat LA, Schwarzacher SW, Cuntz H, Jedlicka P. T2N as a new tool for robust electrophysiological modeling demonstrated for mature and adult-born dentate granule cells. *elife*. 2017:6:e26517.

Belichenko PV, Masliah E, Kleschevnikov AM, Villar AJ, Epstein CJ, Salehi A, Mobley WC. Synaptic structural abnormalities in the Ts65Dn mouse model of down syndrome. *J Comp Neurol*. 2004:480:281–298.

Bieri KW, Bobbitt K, Colgin LL. Slow and fast $\gamma$ rhythms coordinate different spatial coding modes in hippocampal place cells. *Neuron*. 2014:82(3):670–681.

Bindu B, Alladi PA, Mansooralikhan BM, Srikumar BN, Raju TR, Kutty BM. Short-term exposure to an enriched environment enhances dendritic branching but not brain-derived neurotrophic factor expression in the hippocampus of rats with ventral subicular lesions. *Neuroscience*. 2007:144:412–423.

Bonnier C. Evaluation of early stimulation programs for enhancing brain development. *Acta Paediatr*. 2008:97:853–858.

Bonnycastle K, Davenport EC, Cousin MA. Presynaptic dysfunction in neurodevelopmental disorders: insights from the synaptic vesicle life cycle. *J Neurochem*. 2021:157:179–207.

Brady ML, Jacob TC. Synaptic localization of $\alpha$5 GABA (a) receptors via Gephyrin interaction regulates dendritic outgrowth and spine maturation. *Dev Neurobiol*. 2015:75:1241–1251.

Branco T, Häusser M. Synaptic integration gradients in single cortical pyramidal cell dendrites. *Neuron*. 2011:69:885–892.

Branco T, Clark BA, Häusser M. Dendritic discrimination of temporal input sequences in cortical neurons. *Science*. 2010:329:1671–1675.

Broadbent NJ, Gaskin S, Squire LR, Clark RE. Object recognition memory and the rodent hippocampus. *Learn Mem*. 2009:17:5–11.

Chklovskii DB, Schikorski T, Stevens CF. Wiring optimization in cortical circuits. *Neuron*. 2002:2010(34):341–347.

Colgin LL, Denninger T, Fyhn M, Hafting T, Bonnevie T, Jensen O, Moser M-B, Moser EI. Frequency of gamma oscillations routes flow of information in the hippocampus. *Nature*. 2009:462:353–357.

Combe CL, Canavier CC, Gasparini S. Intrinsic mechanisms of frequency selectivity in the proximal dendrites of CA1 pyramidal neurons. *J Neurosci*. 2018:38:8110–8127.

Contestabile A, Magara S, Cancedda L. The GABAergic hypothesis for cognitive disabilities in down syndrome. *Front Cell Neurosci*. 2017:11:54.

Cuntz H, Forstner F, Borst A, Häusser M. The TREES toolbox—probing the basis of axonal and dendritic branching. *Neuroinformatics*. 2011:9:91–96.

De Toma I, Ortega M, Aloy P, Sabidó E, Dierssen M. DYRK1A overexpression alters cognition and neural-related proteomic pathways in the hippocampus that are rescued by green tea extract and/or environmental enrichment. *Front Mol Neurosci*. 2019:12:272.

Dierssen M. Down syndrome: the brain in trisomic mode. *Nat Rev Neurosci*. 2012:13:844–858.

Dierssen M, Ramakers GJA. Dendritic pathology in mental retardation: from molecular genetics to neurobiology. *Genes Brain Behav*. 2006:5(Suppl 2):48–60.

Dierssen M, Benavides-Piccione R, Martínez-Cué C, Estivill X, Flórez J, Elston GN, DeFelipe J. Alterations of neocortical pyramidal cell phenotype in the Ts65Dn mouse model of down syndrome: effects of environmental enrichment. *Cereb Cortex*. 2003:13: 758–764.

Elston GN, Rosa MG. The occipitoparietal pathway of the macaque monkey: comparison of pyramidal cell morphology in layer III of functionally related cortical visual areas. *Cereb Cortex*. 1997:7: 432–452.

Elston GN, Benavides-Piccione R, DeFelipe J. The pyramidal cell in cognition: a comparative study in human and monkey. *J Neurosci*. 2001:21:RC163.

Emoto K. Signaling mechanisms that coordinate the development and maintenance of dendritic fields. *Curr Opin Neurobiol*. 2012:22: 805–811.

Encinas JM, Michurina TV, Peunova N, Park JH, Tordo J, Peterson DA, Fishell G, Koulakov A, Enikolopov G. Division-coupled astrocytic differentiation and age-related depletion of neural stem cells in the adult hippocampus. *Cell Stem Cell*. 20116:8(5):566–579.

Etter G, van der Veldt S, Manseau F, Zarrinkoub I, Trillaud-Doppia E, Williams S. Optogenetic gamma stimulation rescues memory impairments in an Alzheimer's disease mouse model. *Nat Commun*. 2019:10:5322.

Feng L, Zhao T, Kim J. neuTube 1.0: a new Design for Efficient Neuron Reconstruction Software Based on the SWC format. *eNeuro*. 2015:2(1):2–10.

Fernandez F, Garner CC. Episodic-like memory in Ts65Dn, a mouse model of down syndrome. *Behav Brain Res*. 2008:188:233–237.

Fernandez F, Morishita W, Zuniga E, Nguyen J, Blank M, Malenka RC, Garner CC. Pharmacotherapy for cognitive impairment in a mouse model of down syndrome. *Nat Neurosci*. 2007:10:411–413.

Ferrante M, Migliore M, Ascoli GA. Feed-forward inhibition as a buffer of the neuronal input-output relation. *Proc Natl Acad Sci*. 2009:106: 18004–18009.

Flores-Soto M, Romero-Guerrero C, Vázquez-Hernández N, Tejeda-Martínez A, Martín-Amaya-Barajas FL, Orozco-Suárez S, González-Burgos I. Pentylenetetrazol-induced seizures in adult rats are associated with plastic changes to the dendritic spines on hippocampal CA1 pyramidal neurons. *Behav Brain Res*. 2021:406:113198.

Giusi G, Facciolo RM, Rende M, Alò R, Di Vito A, Salerno S, Morelli S, De Bartolo L, Drioli E, Canonaco M. Distinct $\alpha$ subunits of the GABAA receptor are responsible for early hippocampal silent neuron-related activities. *Hippocampus*. 2009:19:1103–1114.

Guedj F, Sébrié C, Rivals I, Ledru A, Paly E, Bizot JC, Smith D, Rubin E, Gillet B, Arbones M, et al. Green tea polyphenols Rescue of Brain Defects Induced by overexpression of DYRK1A. *PLoS One*. 2009:4:e4606.

Himpel S, Tegge W, Frank R, Leder S, Joost HG, Becker W. Specificity determinants of substrate recognition by the protein kinase DYRK1A. *J Biol Chem*. 2000:275:2431–2438.

Jarsky T, Roxin A, Kath WL, Spruston N. Conditional dendritic spike propagation following distal synaptic activation of hippocampal CA1 pyramidal neurons. *Nat Neurosci*. 2005:8:1667–1676.

Jessberger S, Clark RE, Broadbent NJ, Clemenson GD Jr, Consiglio A, Lie DC, Squire LR, Gage FH. Dentate gyrus-specific knockdown of adult neurogenesis impairs spatial and object recognition memory in adult rats. *Learn Mem*. 2009:16(2):147–154.

Johansson BB, Belichenko PV. Neuronal plasticity and dendritic spines: effect of environmental enrichment on intact and postischemic rat brain. *J Cereb Blood Flow Metab*. 2002:22:89–96.

Katz Y, Menon V, Nicholson DA, Geinisman Y, Kath WL, Spruston N. Synapse distribution suggests a two-stage model of dendritic integration in CA1 pyramidal neurons. *Neuron*. 2009:63: 171–177.

Kempermann G, Kuhn H, Gage F. More hippocampal neurons in adult mice living in an enriched environment. *Nature*. 1997:386: 493–495.

Kim S, Guzman SJ, Hu H, Jonas P. Active dendrites support efficient initiation of dendritic spikes in hippocampal CA3 pyramidal neurons. *Nat Neurosci*. 2012:15:600–606.

Kleschevnikov AM, Belichenko PV, Villar AJ, Epstein CJ, Malenka RC, Mobley WC. Hippocampal long-term potentiation suppressed by increased inhibition in the Ts65Dn mouse, a genetic model of down syndrome. *J Neurosci*. 2004:24:8153–8160.

Kurt MA, Kafa MI, Dierssen M, Davies DC. Deficits of neuronal density in CA1 and synaptic density in the dentate gyrus, CA3 and CA1, in a mouse model of down syndrome. *Brain Res*. 2004:1022: 101–109.

Larkum ME, Nevian T, Sandler M, Polsky A, Schiller J. Synaptic integration in tuft dendrites of layer 5 pyramidal neurons: a new unifying principle. *Science*. 2009:325:756–760.

Lipina TV, Prasad T, Yokomaku D, Luo L, Connor SA, Kawabe H, Wang YT, Brose N, Roder JC, Craig AM. Cognitive deficits in Calsyntenin-2-deficient mice associated with reduced GABAergic transmission. *Neuropsychopharmacology*. 2016:41:802–810.

Mahoney G, Perales F, Wiggers B, Herman B. Responsive teaching: early intervention for children with down syndrome and other disabilities. *Downs Syndr Res Pract*. 2006:11:18–28.

Marti E, Altafaj X, Dierssen M, de la Luna S, Fotaki V, Alvarez M, Pérez-Riba M, Ferrer I, Estivill X. Dyrk1A expression pattern supports specific roles of this kinase in the adult central nervous system. *Brain Res*. 2003:964:250–263.

Martinez de Lagran M, Benavides-Piccione R, Ballesteros-Yañez I, Calvo M, Morales M, Fillat C, Defelipe J, Ramakers GJA, Dierssen M. Dyrk1A influences neuronal morphogenesis through regulation of cytoskeletal dynamics in mammalian cortical neurons. *Cereb Cortex*. 2012:22:2867–2877.

Martínez-Cué C, Baamonde C, Lumbreras M, Paz J, Davisson MT, Schmidt C, Dierssen M, Flórez J. Differential effects of environmental enrichment on behavior and learning of male and female Ts65Dn mice, a model for down syndrome. *Behav Brain Res*. 2002:134:185–200.

Megias M, Emri Z, Freund TF, Gulyás AI. Total number and distribution of inhibitory and excitatory synapses on hippocampal CA1 pyramidal cells. *Neuroscience*. 2001:102:527–540.

Milstein AD, Bloss EB, Apostolides PF, Vaidya SP, Dilly GA, Zemelman BV, Magee JC. Inhibitory gating of input comparison in the CA1 microcircuit. *Neuron*. 2015:87:1274–1289.

Munn RGK, Freeburn A, Finn DP, Heller HC. Hyper-rigid phasic Organization of Hippocampal Activity but normal spatial properties of

CA1 place cells in the Ts65Dn mouse model of down syndrome. *J Neurosci*. 2022:42:1542–1556.

Paxinos G, Franklin KBJ. *Paxinos and Franklin's the mouse brain in stereotaxic coordinates*. London, UK: Academic Press; 2019.

Pons-Espinal M, Martinez de Lagran M, Dierssen M. Environmental enrichment rescues DYRK1A activity and hippocampal adult neurogenesis in TgDyrk1A. *Neurobiol Dis*. 2013:60:18–31.

Reynolds GP, Warner CEJ. Amino acid neurotransmitter deficits in adult Down's syndrome brain tissue. *Neurosci Lett*. 1988:94: 224–227.

Risser D, Lubec G, Cairns N, Herrera-Marschitz M. Excitatory amino acids and monoamines in parahippocampal gyrus and frontal cortical pole of adults with down syndrome. *Life Sci*. 1997:60: 1231–1237.

Ruiz-Mejias M, Martinez de Lagran M, Mattia M, Castano-Prat P, Perez-Mendez L, Ciria-Suarez L, Gener T, Sancristobal B, García-Ojalvo J, Gruart A, et al. Overexpression of Dyrk1A, a down syndrome candidate, decreases excitability and impairs gamma oscillations in the prefrontal cortex. *J Neurosci*. 2016:36:3648–3659.

Schaefer AT, Larkum ME, Sakmann B, Roth A. Coincidence detection in pyramidal neurons is tuned by their dendritic branching pattern. *J Neurophysiol*. 2003:89:3143–3154.

Schindelin J, Arganda-Carreras I, Frise E, Kaynig V, Longair M, Pietzsch T, Preibisch S, Rueden C, Saalfeld S, Schmid B, et al. Fiji: an open-source platform for biological-image analysis. *Nat Methods*. 2012:9:676–682.

Shinohara Y, Hosoya A, Hirase H. Experience enhances gamma oscillations and interhemispheric asymmetry in the hippocampus. *Nat Commun*. 2013:4:1652.

Souchet B, Guedj F, Sahún I, Duchon A, Daubigney F, Badel A, Yanagawa Y, Barallobre MJ, Dierssen M, Yu E, et al. Excitation/inhibition balance and learning are modified by Dyrk1a gene dosage. *Neurobiol Dis*. 2014:69:65–75.

Wen Q, Stepanyants A, Elston GN, Grosberg AY, Chklovskii DB. Maximization of the connectivity repertoire as a statistical principle governing the shapes of dendritic arbors. *Proc Natl Acad Sci*. 2009:106:12536–12541.

Zheng C, Bieri KW, Hwaun E, Colgin LL. Fast gamma rhythms in the hippocampus promote encoding of novel object–place pairings. *eNeuro*. 2016:3(2):ENEURO.0001–ENEU16.2016:2–19.

Zorrilla de San Martin J, Delabar J-M, Bacci A, Potier MC. GABAergic over-inhibition, a promising hypothesis for cognitive deficits in down syndrome. *Free Radic Biol Med*. 2018:114: 33–39.